Phase-field simulation for voltage profile of Li_xSn nanoparticle during lithiation/delithiation

Qi Huang [a], Simon Daubner [b,c], Shiwei Zhang [a], Daniel Schneider [b,c], Britta Nestler [b,c], Hong Mao [d], Shuhong Liu [a], Yong Du [a,*]

[a] State Key Lab of Powder Metallurgy, Central South University, 410083 Changsha, China
[b] Institute for Applied Materials (IAM-MMS), Karlsruhe Institute of Technology (KIT), 76131 Karlsruhe, Germany
[c] Institute of Digital Materials Science (IDM), Karlsruhe University of Applied Science, 76133 Karlsruhe, Germany
[d] College of Mechanical Engineering, Hunan Institute of Science and Technology, 414006 Yueyang, China

Keywords:
Tin nanoparticle
Multiphase transition
Phase-concentration equation
Voltage profile
Phase-field method

A B S T R A C T

Tin has become one of the most promising anode materials due to its large theoretical capacity. The multi-phase transformations occurring during the (de-)lithiation process have posed a severe challenge to study their thermodynamic, kinetic and elastic properties via computational methods. In this work, a phase-field framework consisting of phase-concentration equations and Allen-Cahn equations is established. Two concepts to deliver thermodynamic and elasticity data as input quantities for the phase-field model are proposed, namely from density functional theory calculations and the thermodynamic energy of stoichiometric compounds. Using the formulated and configured phase-field model, voltage profiles, composition profiles, phases, and stress distributions of the electrode during the charging/discharging cycles are simulated. The effects of varying applied current densities and the homogeneity/inhomogeneity of the eigenstrain within the electrode on the voltage profile are discussed. According to simulation results, the establishment of stable voltage output remains a challenge under a higher C-rate due to inhomogeneous phase or stress distribution within the nanoparticle. A simulation-based derivation of linkages between electrode morphology, charging rate, stress, and capacity retention could enable an advanced design of electrode microstructures.

1. Introduction

Tin (Sn) and Sn based alloys are among the most promising anode materials for future Li-ion batteries owing to their large theoretical capacity (994mAh/g) [1–3]. However, during lithiation/delithiation, multiple Li_xSn phases appear at different charge stages [4], which are associated with a large volume deformation (300%) [5]. Such a large change in volume poses a challenge to design anodes containing Sn [6]. Many theoretical and experimental efforts have been devoted to investigate the influence of stress distribution [7], plastic deformation [8,9], crack propagation [10–14], the operating voltage (V) [15], capacity [16,17] and migration rate of lithium [18,19] for Sn (or Si) contained anodes.

A lot of fundamental work have been undertaken to investigate the structural, thermodynamic, kinetic, and elastic properties of Li-Sn alloys. The sequence of phase formation in the Li_xSn anode during lithiation is determined by Wen and Huggins [20], which is consistent with the Li-Sn phase diagram [21,22]. These investigations proved that $Li_{0.4}Sn$, LiSn, $Li_{2.333}Sn$, $Li_{2.5}Sn$, $Li_{2.6}Sn$, $Li_{3.5}Sn$ and $Li_{4.4}Sn$ (or $Li_{4.25}Sn$) phases are formed in Sn anode during the operation of the battery. Among them, only $Li_{0.4}Sn$ and LiSn (lithium-poor) phases could be distinguished at room temperature clearly [15,16,23,24]. This observation indicated that the lithium-rich phases are more unstable than lithium-poor phases due to their huge volume change and low migration rate of lithium in phase transition. Besides these observations, in order to investigate the voltage performance of Sn anode in battery operation, Courtney et al. [25] computed the total energies for Li_xSn alloys by means of density functional theory (DFT) calculations for the sake of establishing the Li-Sn voltage profile. However, due to the influence of mechanical energy caused by the huge volume deformation in the Li_xSn electrode during its lithiation/delithiation process, their calculated results deviate from experimental voltage noticeably. The work was further refined by Zhang et al. [26], who investigated the elastic properties of Li-Sn phases through DFT calculations. Their results show that

* Corresponding author.
E-mail address: yong-du@csu.edu.cn (Y. Du).

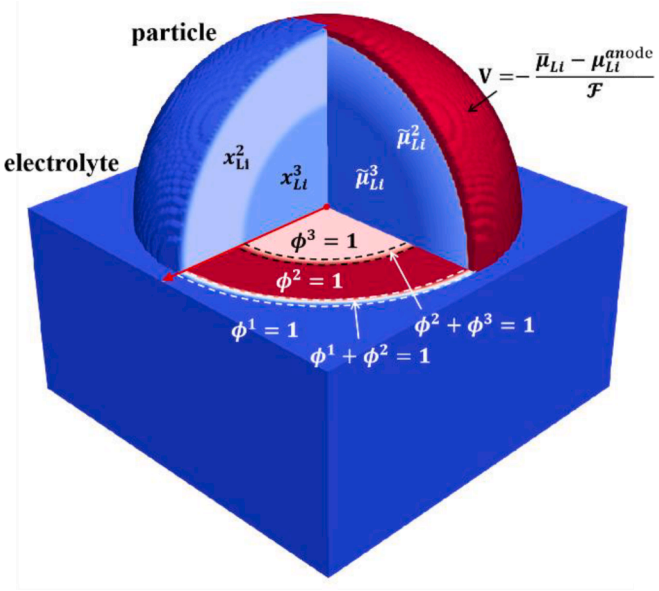

Fig. 1. 3D modeling of the Li_xSn nanoparticle: distribution of two types of field variables (phase volume fraction ϕ^{α} and phase concentration x_i^{α}) and calculation of V (operating voltage) from the averaged chemical potential of lithium. $\phi^n (n \quad 1,2,3)$ is the fraction of phase n. x_{Li}^n and $\tilde{\mu}_{Li}^n$ $(n \quad 1,2,3)$ are the concentration of lithium and the electro-chemo-mechanical potential of lithium in phase n, respectively.

the calculated voltage plateau is in better agreement with the experimental data [27] in comparison with that from Courtney et al. [25]. Chen et al. [19] have measured the kinetic and stress evolutions during potentiostatic lithiation of Sn thin film layers to form the first lithiated phase ($Li_{0.4}Sn$). Modeling the concentration profile, they subsequently fitted the kinetic parameters. It is worth mentioning that Lopez et al. [4], Mukhopadhyay et al. [8], Zhou et al. [14], Beaulieu et al. [15] and Courtney et al. [25] measured the voltage profiles of Li_xSn electrodes, which can be used as a validation for simulations of Li_xSn nanoparticle.

Correlating the electrochemical performance of the whole cell during cycling with the microstructural evolution of individual Sn particles is a challenge [14]. Many advanced methods [24,28–30] have been developed in the past few years to investigate the microstructural evolution of electrode materials in in situ or in operando cell setups during battery operation [31–34]. The computational approaches to simulate the evolution of phases, concentrations, stresses and energy densities during battery operation can provide another perspective to investigate the properties and mechanisms of materials [35,36]. The phase-field method is one of the important modeling methodologies, which is based on energy minimization theory for simulating the dynamic evolution of microstructures [37–40]. This method has been widely used for the theoretical study and microstructure simulation of electrodes for the past decades [41–48]. As the energy density and the diffusion potential of the components can be naturally solved, the voltage profile of the cell can be obtained while simulating the microstructure of electrodes [49–51]. We employ an approach based on Allen-Cahn equations for the evolution of phase volume fractions coupled with phase-dependent concentrations [52] and stresses [40,53]. As the numerically resolved interfacial width is above the scale of natural diffuse interfaces, special care must be taken to avoid excess chemical energy within the interfacial region. Kim et al. [54,55] came forward with a phase-field model where the local components can be decomposed into phase-dependent components and, simultaneously, assuming equal chemical potential of each phase-dependent component within the interface. While this approach is computationally expensive, it has been refined by Plapp [56] who proposed a grand-potential functional to evolve chemical potential directly in a solid–liquid system. This framework has been extended to multiphase systems by Choudhury and Nestler [57] and has recently been introduced for phase-field simulations of electrode materials by Daubner et al. [58,59]. Steinbach et al. [60,61], on the other hand, account for the kinetic relaxation of diffusion potentials within the diffuse interface (interface dissipation) and proposed the finite-interface-dissipation model which can simulate rapid phase transformations, interfaces driven far from equilibrium and the chemical potential jump across the interface. The approaches mentioned above make it possible to evolve the distribution of components during multiphase transitions when coupling thermodynamic databases. Considering that Kim's method is computationally expensive on multiphase junction or in multicomponent system, Choudhury's approach is applicable to solve problems in multiphase without chemical potential jump and Steinbach's model handles mainly diffusion and dissipation processes in alloy systems, it is worthwhile to establish a more general evolution equation for components in each phase that can describe diffusion and chemical reactions (where dissipation can be considered as a special case of the reaction on interface). Consequently, this equation can be used to describe the complex processes of substance migration and chemical reactions within the battery system.

Due to the complex correlation among the operating voltage, thermodynamics, kinetic properties as well as stresses of electrode materials, it is a challenging and meaningful task to effectively couple phase-field model with thermodynamic, kinetic, and elastic data for the simulation of multiphase transition in Sn-contained anodes. To bridge the gap between the phase-concentration equation and the general chemical reaction processes, in Section 2.1.1 and 2.1.2, a self-consistent multiphase and phase-concentration framework based on the Allen-Cahn and mass-conservation equations are derived. The accuracy of the phase-concentration field is proved in Appendix A by comparing with those calculated by mass-conservation equation. To solve the mechanical equilibrium of the system with elastic and structural inhomogeneities, the phase-field microelasticity theory is used, which is discussed in Section 2.1.3. To couple phase-field method with thermodynamic, kinetic, and elastic properties of the stoichiometric compounds (Li_xSn), in Section 2.2 and Appendix B, the eigenstrain model and the Gibbs energy expression are presented, which are further discussed in Section 4. In view of the long time required for phase-field simulation and the high accuracy required for the evolution of the phase-concentration equation while computing operating voltage, some simplifications were suggested to save computational effort, which is described in detail in Section 2.2 and Appendix C. The presently established framework is validated through the experimental results from the previous literature work in Section 3. Finally, the effects of stress and phase distribution on the voltage stability of sn-contained electrodes during lithiation/delithiation are investigated. The mechanism of output voltage instability is revealed.

2. Material and methods

2.1. Multiphase field framework

Fig. 1 schematically shows the representative microstructure of the Li_xSn nanoparticles chosen for our model. A spherical Li_xSn particle is located in the center of the simulated domain, while the remaining domain is filled with an electrolyte. Assuming that there is no phase transition between the solid particle and the electrolyte, the evolution of the substances in electrolyte is not considered in this work. In order to describe the multiphase transition and substance migration processes within the particle, two types of field variables (the phase volume fraction $\phi^{\alpha}(\boldsymbol{r},t)$ and the phase-dependent concentration $x^{\alpha}(\boldsymbol{r},t)$) are introduced. We assume that the molar fraction ($x^{\alpha}, x^{\beta}, \ldots$) in each phase are independent variables [61] and, furthermore, that the diffusion potentials of all phases are equal in final equilibrium state. During cell operation, the difference in diffusion potentials drives the electrode

reaction on nanoparticle's surface and the dissipation between solid phases, which are modelled employing the Butler-Volmer equation and linear reaction kinetics. To correctly describe the driving force and diffusion potential in the nanoparticle, in this section, the variational analysis of the total energy with respect to ϕ^α and x^α is performed first. Then, the Allen-Cahn and the mass-conservation equations will be further derived into the summation of pair-wise phase transformations and the phase-concentration equation form.

2.1.1. Energy functional

The total free energy of the whole system is described by the Ginzburg-Landau form

$$F = \int_V f_{total} d^3 r = \int_V (f_{int} + f_{chem} + f_{elas} + f_{elec}) d^3 r, \tag{1}$$

$$f_{int} = \sum_{\alpha,\beta>\alpha} \xi^{\alpha\beta} \left(\frac{16}{\varepsilon \pi^2} \phi^\alpha \phi^\beta \quad \varepsilon \left| \phi^\alpha \nabla \phi^\beta \quad \phi^\beta \nabla \phi^\alpha \right|^2 \right), \tag{2}$$

$$f_{chem} = (V_m)^{-1} \sum_\alpha \phi^\alpha G_m^\alpha \left(x_i^\alpha, T \right), \tag{3}$$

$$f_{elas} = \frac{1}{2} [\epsilon \quad \epsilon^*(\phi, x)] : C^{eff}(\phi) : [\epsilon \quad \epsilon^*(\phi, x)], \tag{4}$$

$$f_{elec} = \mathscr{F} (V_m)^{-1} \sum_\alpha \left(\phi^\alpha \varphi^\alpha \sum_i z_i^\alpha x_i^\alpha \right), \tag{5}$$

where λ_i is the Laplace operator for component i.

When the phase-dependent concentration evolves to the equilibrium state, the variation of Γ to x_i^α should vanish such that

$$\frac{\delta}{\delta x_i^\alpha} \Gamma = 0 = \frac{\delta}{\delta x_i^\alpha} f_{total} \quad \phi^\alpha \lambda_i. \tag{7}$$

The same derivation can be applied to the same components in each phase (x_i^α, x_i^β, …), and the following relationship exists at equilibrium state

$$\lambda_i = \frac{1}{\phi^\alpha} \frac{\delta}{\delta x_i^\alpha} f_{total} = \frac{1}{\phi^\beta} \frac{\delta}{\delta x_i^\beta} f_{total} = \cdots. \tag{8}$$

Based on eqs. (6–8), the driving force for the evolution of phase-dependent concentration in non-equilibrium state, which is named as diffusion potential, can be given as

$$\begin{aligned} \tilde{\mu}_i^\alpha (V_m)^{-1} &= \lambda_i = \frac{1}{\phi^\alpha} \frac{\delta}{\delta x_i^\alpha} f_{total} \\ &= \frac{\partial G_m^\alpha}{\partial x_i^\alpha} (V_m)^{-1} + F z_i^\alpha \varphi^\alpha (V_m)^{-1} \quad \frac{\partial \epsilon^{*,\alpha}}{\partial x_i^\alpha} : C^{eff} : [\epsilon \quad \epsilon^*] + \frac{1}{2} [\epsilon \quad \epsilon^*] : \frac{\partial C^{eff}}{\partial x_i^\alpha} : [\epsilon \quad \epsilon^*]. \end{aligned} \tag{9}$$

Generally, the phase-dependent electric potential is assumed as constant across the electrode active material for the fast motion of electrons.

Then, the variation of the Γ with respect to phase volume fraction, yields

$$\begin{aligned} \frac{\delta}{\delta \phi^\alpha} \Gamma &= \frac{\delta}{\delta \phi^\alpha} f_{total} \quad \sum_{i=1}^{n-1} \tilde{\mu}_i^\alpha (V_m)^{-1} x_i^\alpha \\ &= \left(\frac{\partial}{\partial \phi^\alpha} \quad \nabla \cdot \frac{\partial}{\partial \nabla \phi^\alpha} \right) f_{int}(\phi, \nabla \phi) + G_m^\alpha (V_m)^{-1} + \frac{1}{2} (\epsilon_{mn} \quad \epsilon_{mn}^*) C_{mnop}^\alpha \left(\epsilon_{op} \quad \epsilon_{op}^* \right) \quad \sigma_{op} \epsilon_{op}^{*,\alpha} \\ &\quad \sum_{i=1}^{n-1} \left[\frac{\partial G_m^\alpha}{\partial x_i^\alpha} (V_m)^{-1} \quad \frac{\partial \epsilon_{mn}^{*,\alpha}}{\partial x_i^\alpha} \sigma_{mn} + \frac{1}{2} (\epsilon_{mn} \quad \epsilon_{mn}^*) \frac{\partial C_{mnop}^\alpha}{\partial x_i^\alpha} \left(\epsilon_{op} \quad \epsilon_{op}^* \right) \right] x_i^\alpha. \end{aligned} \tag{10}$$

where f_{int}, f_{chem}, f_{elas} and f_{elec} are the interfacial [39,62], chemical [63], elastic [64], and electrical [41] energy densities in local, respectively. $\xi^{\alpha\beta}$ is the energy density of α and β interface. ε controls the diffuse interface thickness at all phase boundaries within the phase-field model. $G_m^\alpha(x_i^\alpha, T)$ is the Gibbs free energy of α phase. V_m is the molar volume. ϵ is the total strain which can be solved from mechanical equilibrium condition. $C^{eff}(\phi, x)$ and $\epsilon^*(\phi, x)$ can be assumed to be linear interpolations of phase-dependent stiffnesses $C^{eff}(\phi) = \sum_\alpha \phi^\alpha C^\alpha$ and eigenstrains $\epsilon^*(\phi, x) = \sum_\alpha \phi^\alpha \epsilon^{*,\alpha}(x^\alpha)$, respectively. φ^α is the phase-dependent electric potential. $\mathscr{F}$ is the faraday constant. And z_i^α is the number of charges of component i in α phase. According to the definition of eqs. (3–5), the bulk free energy density comprises the chemical, mechanical as well as electrical energies such that $f_{bulk} = f_{chem} + f_{elas} + f_{elec}$.

It is assumed that the simulation system contains n components, which are given by the total concentration $x_i(\boldsymbol{r}, t)$, the relationship $\sum_i x_i = 1$ holds and n 1 of them are independent. Besides, to ensure the substances conservation, $x_i(\boldsymbol{r}, t)$ can be obtained by a mixture rule $x_i(\boldsymbol{r}, t) = \sum_\alpha \phi^\alpha(\boldsymbol{r}, t) x_i^\alpha(\boldsymbol{r}, t)$. This relationship is introduced here as a constraint to enable these two kinds of field variables are energetically related [61]

$$\Gamma = f_{total} + \sum_{i=1}^{n-1} \lambda_i \left(x_i \quad \sum_\alpha \phi^\alpha x_i^\alpha \right). \tag{6}$$

2.1.2. Multiphase evolution equation

The evolution of the phase-concentration equation is closely related to the evolution of the multiphase equation, which requires the normalization of phases ($\sum_\alpha \phi^\alpha = 1$). Introducing this relationship as a constraint into the Allen-Cahn equation

$$\frac{\partial \phi^\alpha}{\partial t} = L^\alpha \frac{\delta}{\delta \phi^\alpha} \left[f_{total} + \lambda_\phi \left(\sum_\gamma \phi^\gamma \quad 1 \right) \right] = L^\alpha \frac{\delta}{\delta \phi^\alpha} f_{total} \quad L^\alpha \lambda_\phi, \tag{11}$$

where L^α is the evolution rate of α phase and λ_ϕ is a Lagrange parameter for the constraint $\sum_\alpha \phi^\alpha = 1$. Since local phases are normalized, the following relationship exists [62]

$$0 = \sum_\alpha \frac{\partial \phi^\alpha}{\partial t} = \quad \sum_\alpha \left(L^\alpha \frac{\delta}{\delta \phi^\alpha} f_{total} + L^\alpha \lambda_\phi \right). \tag{12}$$

Then, λ_ϕ can be obtained

$$\lambda_\phi = \quad \frac{1}{N} \sum_\alpha \frac{\delta}{\delta \phi^\alpha} f_{total}, \tag{13}$$

By substituting Eq. (13) into Eq. (11), the multiphase evolution equation can finally be derived [65]

$$\frac{\partial \phi^{\alpha}}{\partial t}=\frac{L^{\alpha}}{N}\sum_{\beta\neq\alpha}\left(\frac{\delta}{\delta\phi^{\beta}}\quad\frac{\delta}{\delta\phi^{\alpha}}\right)f_{total}=\frac{1}{N}\sum_{\beta\neq\alpha}\tilde{L}^{\alpha\beta}\left(\frac{\delta}{\delta\phi^{\beta}}\quad\frac{\delta}{\delta\phi^{\alpha}}\right)f_{total}, \tag{14}$$

where N is the local number of phases, $\tilde{L}^{\alpha\beta}$ the migration rate of interface of α and β phases ($\partial\Omega^{\alpha\beta}$). For the application of the above model formulation, in this work, we assume that the volume of Li_xSn particle will not change. Therefore, the migration rate of interface between particle and electrolyte is set to zero during simulation.

2.1.3. Phase-Concentration evolution equation

The general form of the mass-conservation equation for α phase is given as follows based on the Fick's second law

$$(V_m)^{-1}\frac{\partial x_i^{\alpha}}{\partial t}=\quad\nabla\cdot\boldsymbol{J_i^{\alpha}}+S_i^{\alpha}=\nabla\cdot\left(\sum\nolimits_{j=1}^{n}M_{ij}^{\alpha}\nabla\overset{\sim}{\mu}_j^{\alpha}\right)+S_i^{\alpha}, \tag{15}$$

where x_i^{α} is the phase concentration of component i, $\boldsymbol{J_i^{\alpha}}$ the flux term, S_i^{α} the source term, M_{ij}^{α} correlated chemical mobilities, $\mu\overset{\sim}{}_j^{\alpha}$ the diffusion potential of component i. This diffusion equation works in simulation domain filled with α phase. In order to derive it into a form applicable to multiphase frameworks, referring to the work of Yu et al. [66], we multiply Eq. (15) by ϕ^{α}. The phase fraction ϕ^{α} describes the domain in which diffusion occurs. The diffusion equation for α phase with smooth boundary can be obtained

$$(V_m)^{-1}\phi^{\alpha}\frac{\partial x_i^{\alpha}}{\partial t}=\phi^{\alpha}\nabla\cdot\boldsymbol{J_i^{\alpha}}+\phi^{\alpha}S_i^{\alpha}=\nabla\cdot\left(\phi^{\alpha}\boldsymbol{J_i^{\alpha}}\right)\quad\nabla\phi^{\alpha}\cdot\boldsymbol{J_i^{\alpha}}+\phi^{\alpha}S_i^{\alpha}, \tag{16}$$

where the first item $\nabla\cdot\left(\phi^{\alpha}\boldsymbol{J_i^{\alpha}}\right)$ describes diffusion fluxes within the bulk phase, the second item $\nabla\phi^{\alpha}\cdot\boldsymbol{J_i^{\alpha}}$ describes inward diffusion fluxes at the phase boundary. The mixing rule $x_i(\boldsymbol{r},t)=\sum_{\alpha}\phi^{\alpha}(\boldsymbol{r},t)x_i^{\alpha}(\boldsymbol{r},t)$ shows that the total concentration is related to $\phi^{\alpha}(\boldsymbol{r},t)$ and $x_i^{\alpha}(\boldsymbol{r},t)$, which means that the phase change also affects the phase concentration. To establish this relationship, we assume that the total concentration in each phase $\phi^{\alpha}(\boldsymbol{r},t)x_i^{\alpha}(\boldsymbol{r},t)$ remains constant during the phase transition process

$$\frac{\partial\left[\phi^{\alpha}(\boldsymbol{r},t)x_i^{\alpha}(\boldsymbol{r},t)\right]}{\partial t}=0=\phi^{\alpha}(\boldsymbol{r},t)\frac{\partial x_i^{\alpha}(\boldsymbol{r},t)}{\partial t}+x_i^{\alpha}(\boldsymbol{r},t)\frac{\partial\phi^{\alpha}(\boldsymbol{r},t)}{\partial t}. \tag{17}$$

Adding the increment of phase concentration caused by phase transition into Eq. (16), the phase-concentration evolution equation in multiphase framework can be developed as

$$(V_m)^{-1}\frac{\partial x_i^{\alpha}}{\partial t}=\frac{1}{\phi^{\alpha}}\left[\nabla\cdot\left(\phi^{\alpha}\boldsymbol{J_i^{\alpha}}\right)\quad\nabla\phi^{\alpha}\cdot\boldsymbol{J_i^{\alpha}}+\phi^{\alpha}S_i^{\alpha}\quad(V_m)^{-1}x_i^{\alpha}\frac{\partial\phi^{\alpha}}{\partial t}\right]. \tag{18}$$

Eqs. (16) and (17) implies that the diffusion of the components at the phase boundary has a large impact on the phase transition, which makes Eq. (18) more suitable for simulating diffusion-controlled phase transition processes.

In Eq. (2), the boundary gradient of pair-wise phases $\nabla\phi^{\alpha\beta}=\phi^{\beta}\nabla\phi^{\alpha}\quad\phi^{\alpha}\nabla\phi^{\beta}$ is defined. Based on which, the unit inward normal vector of pair-wise phases can be written as $\boldsymbol{n^{\alpha\beta}}=\quad\nabla\phi^{\alpha\beta}/\left|\nabla\phi^{\alpha\beta}\right|$. The constraint $\sum_{\alpha}\phi^{\alpha}=1$ introduced in Eq. (11) makes it possible to derive $\nabla\phi^{\alpha}\cdot\boldsymbol{J_i^{\alpha}}$ in the form of a summary of diffusion fluxes at the boundary of each pair-wise phases:

$$\nabla\phi^{\alpha}\cdot\boldsymbol{J_i^{\alpha}}\qquad\sum_{\beta\neq\alpha}\nabla\phi^{\alpha\beta}\cdot\boldsymbol{J_i^{\alpha}}=\quad\sum_{\beta\neq\alpha}\left(\nabla\phi^{\alpha\beta}\cdot\overset{\sim}{\boldsymbol{J}}_i^{\alpha\beta}\right)\quad\sum_{\beta}\left|\nabla\phi^{\alpha\beta}\right|\left(\boldsymbol{n^{\alpha\beta}}\cdot\overset{\sim}{\boldsymbol{J}}_i^{\alpha\beta}\right), \tag{19}$$

where $\overset{\sim}{\boldsymbol{J}}_i^{\alpha\beta}$ is the diffusion flux of component i at the phase boundary of α-β pair-wise phases, and $\boldsymbol{n^{\alpha\beta}}\cdot\overset{\sim}{\boldsymbol{J}}_i^{\alpha\beta}$ the inward diffusion flux or reaction at the phase boundary of α-β pair-wise phases.

The above model formulation is applied to model lithium within the Sn solid phase, i.e., we can reduce the formulation to the molar fraction of Li. Due to the occurring phase transformations, we introduce the five field variables $x_{\mathrm{Li}}^{\mathrm{Sn}}$, $x_{\mathrm{Li}}^{\mathrm{Li_{0.4}Sn}}$, $x_{\mathrm{Li}}^{\mathrm{LiSn}}$, $x_{\mathrm{Li}}^{\mathrm{Li_{2.6}Sn}}$ and $x_{\mathrm{Li}}^{\mathrm{Li_{3.5}Sn}}$. The five phases given are solid phases within particle, in which there is diffusion of substances in each phase and dissipation of substances at the interface of two solid phases. The dissipation process (e.g., $Li_{\alpha}\leftrightharpoons Li_{\beta}$) is modelled employing linear reaction kinetics at solid–solid interfaces

$$\boldsymbol{n^{\alpha\beta}}\cdot\overset{\sim}{\boldsymbol{J}}_{\mathbf{Li}}^{\alpha\beta}=\kappa_{\mathrm{Li}}^{\alpha\beta}\left(\overset{\sim}{\mu}_{\mathrm{Li}}^{\beta}\quad\overset{\sim}{\mu}_{\mathrm{Li}}^{\alpha}\right), \tag{20}$$

where $\kappa_{\mathrm{Li}}^{\alpha\beta}$ is the dissipation rate. When a solid phase is located on the surface of a particle, there exists an interface between the solid phase and the electrolyte. Although, according to dissipation theory, an open structure will reach equilibrium through the exchange of matter and energy with other structures [67,68], which means that the dissipation process is also present at the electrode surface. For example, some experiments [69–71] have found dissolution of metals in electrodes, resulting in loss of capacity. Since the dissolution of metals in the Li_xSn particle is negligible in this work, the dissipation behavior of the particle surface is not considered here. Instead, the electrode reaction process (e.g. $Li_e^{+}+\boldsymbol{e}\leftrightharpoons Li_s$) driven by the difference of electro-chemo-mechanical potential $\mu\overset{\sim}{}_{\mathrm{Li}}^{e}\quad\overset{\sim}{\mu}_{\mathrm{Li}}^{s}$ between solid phase (s) and electrolyte (e) is significant and considered here assuming Butler-Volmer reaction kinetics [48]

$$\boldsymbol{n^{se}}\cdot\overset{\sim}{\boldsymbol{J}}_{\mathbf{Li}}^{se}=\kappa_{\mathrm{Li}}^{se}\left(x_{\mathrm{Li}^{+}}^{e}\right)^{a}\left(1\quad x_{\mathrm{Li}}^{s}\right)\left(x_{\mathrm{Li}}^{s}\right)^{1-a}\left\{exp\left(\frac{a\eta\mathscr{F}}{RT}\right)\quad exp\left[\quad\frac{(1\quad a)\eta\mathscr{F}}{RT}\right]\right\}, \tag{21}$$

where $\kappa_{\mathrm{Li}}^{se}$ is the electrode reaction rate. The symmetric factor a is assumed as 0.5. R is the ideal gas constant 8.314463 [J·K ^{1}·mol ^{1}]. Under the assumption that the reference electrode is pure Li (p), and the electrode reaction at pure Li surface and the Li^{+} transport in electrolyte are both fast [59], we assume $x_{\mathrm{Li}^{+}}^{e}$ and φ^{e} to be constant around the Li_xSn particle. And the overpotential η can be approximated by

$$\eta=\frac{\mu\overset{\sim}{}_{\mathrm{Li}}^{e}\quad\overset{\sim}{\mu}_{\mathrm{Li}}^{s}}{\mathscr{F}}=\Delta\varphi+\frac{\widehat{\mu}_{\mathrm{Li}}^{p}\quad\widehat{\mu}_{\mathrm{Li}}^{s}}{\mathscr{F}}, \tag{22}$$

where $\widehat{\mu}_{\mathrm{Li}}$ is the chemo-mechanical potential. And, in this work, the applied current is known as a constant during (de-)lithiation process. To investigate the multiphase transition within the Li_xSn particles more clearly, we simplified Eq. (22) in simulation, which is discussed in detail in Section 2.2. Moreover, there are no other chemical reactions within the solid phase, so $S\overset{\sim}{}_i^{\alpha}=0$.

Eq. (18) will naturally reduce to the general mass-conservation equation in bulk. And eqs. (20, 21) works on the interface ($\partial\Omega^{\alpha\beta}$) between two phases (solid phases or electrolyte). Based on the basic knowledge that the rate of grain boundary diffusion is slightly higher than the diffusion within the bulk in alloys. The dissipation rate at grain boundary in electrode can be further evaluated. And considering that the interface width has a significant effect on the accuracy of the result of phase-concentration equation. In Appendix A, the function of the dissipation rate in alloys is derived, and the results evolved by the phase-concentration equation are compared with the standard result of the matter-conservation.

2.1.4. Phase-Field microelasticity theory [40]

In order to investigate the mechanical properties of the Li_xSn electrode particle during battery operation, it is difficult to solve the stress–strain due to the multiphase transitions and large volume changes of the nanoparticle [72]. In general, the finite deformation theory ($\epsilon_{ij}(\boldsymbol{r})=\left(\partial u_i/\partial r_j+\partial u_j/\partial r_i+\partial u_m/\partial r_i\times\partial u_m/\partial r_j\right)/2$) is used to deal with large volume deformation problems. However, for computational efficiency, we introduced a factor ω to numerically constrain the mismatch between the solid phases ($\epsilon^{*}<10\%$). As a result, the term $\partial u_m/\partial r_i\times$

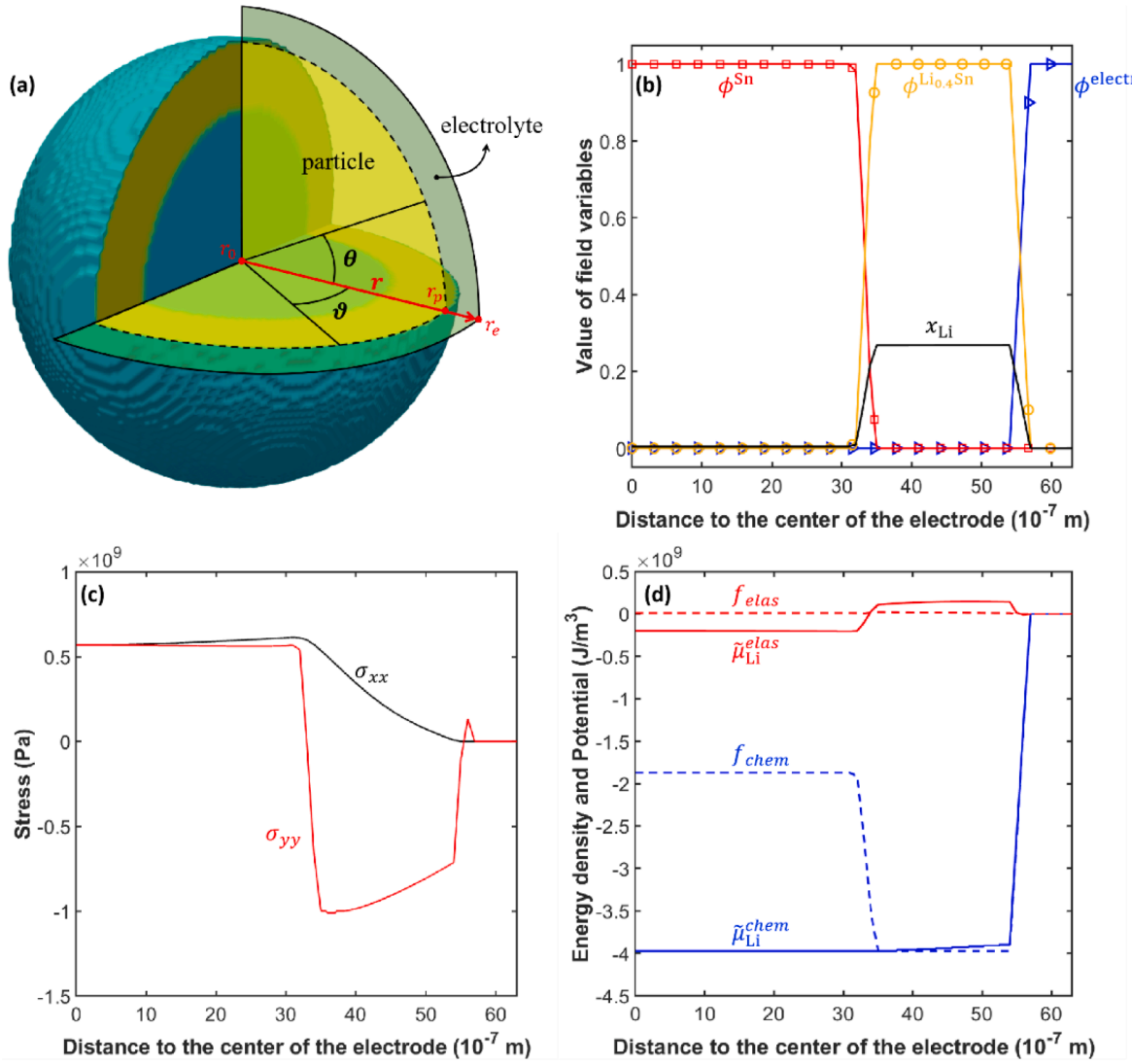

Fig. 2. Calculation Diagram for the nanoparticle model: (a) An axisymmetric nanoelectrode particle is surrounded by the electrolyte; (b, c, and d) The distribution of field variables, stresses, energy densities and diffusion potentials over the radius of the nanoparticle, respectively.

$\partial u_m/\partial r_j$ can be ignored and the small deformation model is used in this work. In addition, the phase-field microelasticity theory [40] (MT) is used to to calculate the stress in the elastically inhomogeneous systems, based on the small strain model, which is required for the solution of the stress–strain within the Li_xSn nanoparticle.

The MT is a semi-implicit computational method which transforms the elastically inhomogeneous system into an elastically homogeneous system and naturally evolves the virtual misfit strain to minimize the mechanical energy [40,73]. Based on this method, the total strain $\epsilon_{ij}(\boldsymbol{r})$ can be given as

$$\epsilon_{ij}(\boldsymbol{r}) = \bar{\epsilon}_{ij} + \frac{1}{2}\int_{|\boldsymbol{k}|\neq 0}\left[n_i\Omega_{jk}(\boldsymbol{n}) + n_j\Omega_{ik}(\boldsymbol{n})\right] \times C^0_{klmn}\tilde{\epsilon}^0_{mn}(\boldsymbol{k})n_l e^{i\boldsymbol{k}\cdot\boldsymbol{r}}\frac{d^3k}{(2\pi)^3}, \quad (23)$$

where C^0_{klmn} is the homogeneous elastic stiffness and $\epsilon^0_{mn}(\boldsymbol{r})$ denotes the virtual misfit strain. The average strain is obtained by $\bar{\epsilon}_{ij} = \int_V \epsilon_{ij}(\boldsymbol{r})d^3r/V$, V represents the system volume, $\boldsymbol{k}$ a wave vector and $|\boldsymbol{k}|$ is its modulus. n_i denotes a component of the unit vector $\boldsymbol{n} = \boldsymbol{k}/|\boldsymbol{k}|$ and $\Omega_{jk}(\boldsymbol{n})$ is the Green function tensor. The Fourier transform of the field $\epsilon^0_{mn}(\boldsymbol{k})$ is represented by $\tilde{\epsilon}^0_{mn}(\boldsymbol{r})$. In Eq. (4), the effective stiffness can always be present as a sum of homogeneous elastic stiffness. The modulus variation $C^{eff}_{ijkl}(\boldsymbol{r}) = C^0_{ijkl} \quad \Delta C_{ijkl}(\boldsymbol{r})$.

It should be noted that the stress $\sigma_{ij}(\boldsymbol{r})$ in the elastically homogeneous system is equal to the stress in the elastically inhomogeneous system

$$C^0_{ijkl}\left[\epsilon_{kl}(\boldsymbol{r}) \quad \epsilon^0_{kl}(\boldsymbol{r})\right] = \sigma_{ij}(\boldsymbol{r}) = \left[C^0_{ijkl} \quad C_{ijkl}(\boldsymbol{r})\right] \times \left[\epsilon_{kl}(\boldsymbol{r}) \quad \epsilon^*_{kl}(\boldsymbol{r})\right]. \quad (24)$$

Moreover, the virtual misfit strain $\epsilon^0_{ij}(\boldsymbol{r})$ is treated as a non-conserved field variable developed by the Allen-Cahn type equation

$$\frac{\partial\epsilon^0_{ij}(\boldsymbol{r},t)}{\partial t} = L_{ijkl}\frac{\delta E^{inhom}}{\delta\epsilon^0_{kl}(\boldsymbol{r},t)}, \quad (25)$$

where t is the virtual time. L_{ijkl} denotes the kinetic coefficient, which governs the rate of the evolution of the virtual misfit strain. E^{inhom} represents the elastic energy of the elastically and structurally inhomogeneous system, which is given by

$$\begin{aligned} E^{inhom} = &\frac{1}{2}\int_V\left[C^0_{ijmn}\Delta C^{-1}_{mnpq}(\boldsymbol{r})C^0_{pqkl} \quad C^0_{ijkl}\right] \times \left[\epsilon^0_{ij}(\boldsymbol{r}) \quad \epsilon^*_{ij}(\boldsymbol{r})\right]\left[\epsilon^0_{kl}(\boldsymbol{r}) \quad \epsilon^*_{kl}(\boldsymbol{r})\right]d^3r \\ &+\frac{1}{2}\int_V C^0_{ijkl}\epsilon^0_{ij}(\boldsymbol{r})\epsilon^0_{kl}(\boldsymbol{r})d^3r \quad \bar{\epsilon}_{ij}\int_V C^0_{ijkl}\epsilon^0_{kl}(\boldsymbol{r})d^3r + \frac{V}{2}C^0_{ijkl}\bar{\epsilon}_{ij}\bar{\epsilon}_{kl} \\ &\frac{1}{2}\int_{|\boldsymbol{k}|\neq 0} n_i\tilde{\sigma}^0_{ij}(\boldsymbol{k})\Omega_{jk}(\boldsymbol{n})\tilde{\sigma}^0_{kl}(\boldsymbol{k})'n_l\frac{d^3k}{(2\pi)^3}, \end{aligned} \quad (26)$$

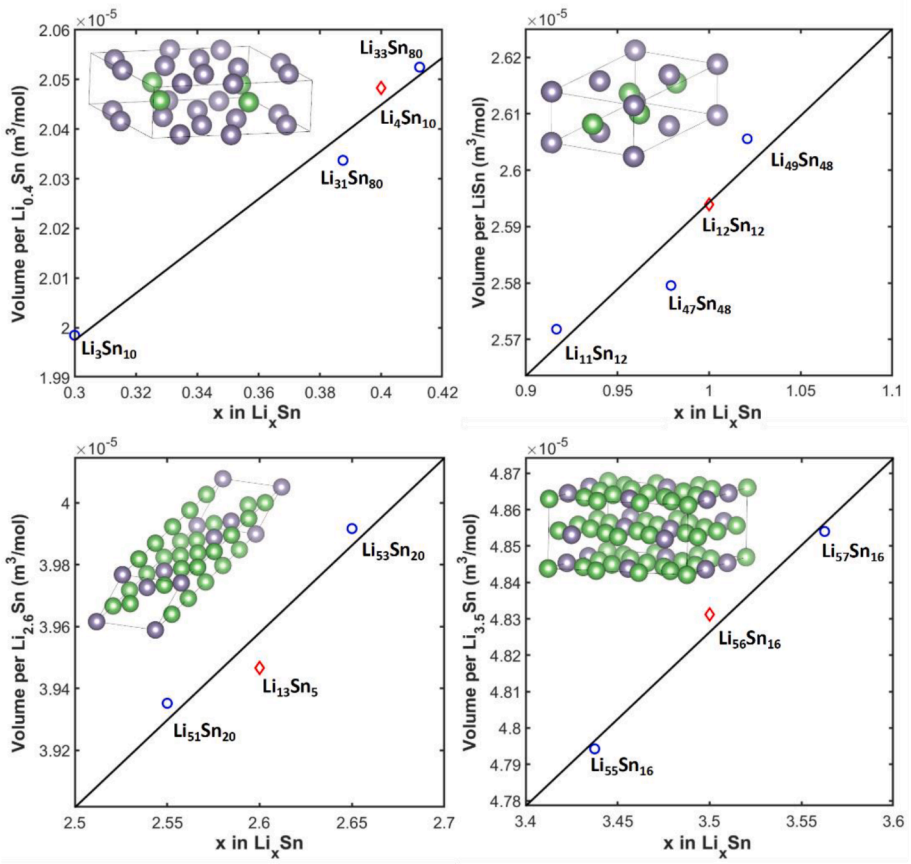

Fig. 3. The volumes of the crystal cells ($Li_{0.4}Sn$, LiSn , $Li_{2.6}Sn$ and $Li_{3.5}Sn$) were changed by the inserting and removing of lithium atoms. The crystal structure of each phase is shown in each diagram, where the green particles are Li atoms and the gray particles are Sn atoms. The functions of volume per Li_xSn can be obtained by fitting the results of DFT calculations. (For interpretation of the references to color in this figure legend, the reader is referred to the web version of this article.)

where $\tilde{\sigma}^0_{ij}(\boldsymbol{k}) = C^0_{ijkl}\tilde{\epsilon}^0_{ij}(\boldsymbol{k})$. The superscript asterisk indicates the complex conjugate. As a result, the stress $\sigma_{ij}(\boldsymbol{r})$ and the total strain $\epsilon_{ij}(\boldsymbol{r})$ can be calculated by eqs. (23 and 24), after evolving $\epsilon^0_{ij}(\boldsymbol{r}, t)$ (by Eq. (25)), until mechanical equilibrium.

3. Calculation

To save computational effort, the field variables (phase volume fraction ϕ^α and phase concentration x_i^α) were solved in the spherically symmetric coordinate, using the finite difference method. The Laplacian and the gradient operators in eqs. (10) and (18) are expressed as

$$\begin{cases} \nabla^2 = \dfrac{1}{r^2}\dfrac{\partial}{\partial r}\left(r^2\dfrac{\partial}{\partial r}\right) \\ \nabla = \dfrac{\partial}{\partial r} \end{cases}, \tag{27}$$

where r is the distance from the center to the calculation point of the sphere. As shown in Fig. 2(a), the point r_0 is the center of the sphere, while the point r_p represents the surface of the nanoparticle and the point r_e denotes the point in the electrolyte. The radius of the nanoparticles $r_p \quad r_0$ is 55×10^{-7}[m] and the simulated domain size $r_e \quad r_0$ is 64×10^{-7}[m]. The electrolyte phase is introduced here to allow the electrode reaction model (as shown in Eq. (21)) to work automatically, and on the other hand to avoid dealing with complex boundary conditions during the mechanical equilibrium solution. There is no phase transition between the electrolyte and the nanoparticle. It is well known that MT is efficient in the calculation of stresses that require periodic boundary conditions. Therefore, in this work, a two-dimensional Cartesian grid of size $128 \times 128 (\times 10^{-7}[\mathrm{m}])$ is defined in this work to solve the stress–strain distribution. Fig. 2(b–d) shows the distribution of field variables, stresses, energy densities and diffusion potentials over the radius of the sphere.

The phase-dependent eigenstrains are given by

$$\epsilon^{*,Li_xSn} = \epsilon^{hom} + \epsilon^{\phi,Li_xSn}(1 \quad \omega) + \epsilon^{x,Li_xSn}, \tag{28a}$$

$$\epsilon^{\phi,\mathrm{Li}_x\mathrm{Sn}} = \left[V_m^{\mathrm{Li}_x\mathrm{Sn}}\left(\frac{x}{x+1}\right)\Big/ V_m^{\mathrm{Sn}}\right]^{1/3} \quad 1, \tag{28b}$$

$$\epsilon^{x,\mathrm{Li}_x\mathrm{Sn}} = \left[V_m^{\mathrm{Li}_x\mathrm{Sn}}\left(x_{\mathrm{Li}}^{\mathrm{Li}_x\mathrm{Sn}}\right)\Big/ V_m^{\mathrm{Li}_x\mathrm{Sn}}\left(\frac{x}{x+1}\right)\right]^{1/3} \quad 1, \tag{28c}$$

where ϵ^{hom} represents the homogeneous eigenstrain of the whole nanoparticle, $\epsilon^{\phi,\mathrm{Li}_x\mathrm{Sn}}$ represents the inhomogeneous eigenstrain of the nanoparticle for the molar volume difference of each phase, and $\epsilon^{x,\mathrm{Li}_x\mathrm{Sn}}$ is the lattice distortion caused by the insertion and de-insertion of lithium atoms in the crystal cell. In Eq. (28), V_m^{Sn} and $V_m^{\mathrm{Li}_x\mathrm{Sn}}$ is the molar volume of Sn and Li_xSn, respectively. Since part of the eigenstrain is an irreversible deformation (e.g., cracking, and plastic deformation, etc.), the relaxation factor ω is introduced to constrain the eigenstrain inhomogeneity.

The volumes of crystal cells for $Li_{0.4}Sn$, LiSn, $Li_{2.6}Sn$ and $Li_{3.5}Sn$ have already been studied [26,74–78]. In present work, the volume change of Li_xSn crystal cell during the process of lithiation/delithiation needs to be further investigated, and therefore density functional theory (DFT) calculations need to be introduced. All the DFT calculations were performed by Vienna Ab initio Simulation Package (VASP) [79] with the projector augmented wave (PAW) method [80] and Perdew-Burke-

Table 1
Elastic constant [26] [GPa] of Li_xSn used in the present simulation.

Elastic constant	Phases				
	Sn	$Li_{0.4}Sn$	LiSn	$Li_{2.6}Sn$	$Li_{3.5}Sn$
C11	56.83	60.08	59.23	78.84	55.33
C22	56.83	60.08	83.17	78.84	70.03
C33	56.83	97.48	65.09	109.0	79.76
C44	25.62	20.44	18.21	21.03	13.64
C55	25.62	20.44	18.08	21.03	34.86
C66	25.62	14.93	19.25	31.38	41.24
C12	27.95	55.75	24.19	16.08	21.64
C13	27.95	19.55	20.23	7.06	17.84
C23	27.95	19.55	24.98	7.06	5.24
C15	–	–	2.4	–	–
C25	–	–	0.44	–	–
C35	–	–	4.1	–	–
C46	–	–	0.87	–	–

Table 2
Formation energies $\Delta G_m^{Li_xSn}\left[kJ \bullet mol^{-1}\right]$ used in the present simulation.

Phases	$Li_{0.4}Sn$	LiSn	$Li_{2.6}Sn$	$Li_{3.5}Sn$
$\Delta G_m^{Li_xSn}$ [a]	20.69	–33.31	40.19	37.31

[a] Reference states [83] are BCC-Li ($G_m^{BCC\_Li}$) and BCT-Sn ($G_m^{BCT\_Sn}$).

Table 3
Summary of the simulation parameters for Li_xSn nanoparticle.

Sym.	Description	Value	Source
Δr	edge length of spatial grid	1×10^{-7}[m]	ref. [25]
$\Delta\widehat{t}$	time interval	auto-change	–
ε	interface width	$4\times dr$	refs. [39,62]
$\xi^{\alpha\beta}$	interface energy for solid phases	$10\left[J\cdot m^{-2}\right]$	ref. [27]
V_m	molar volume	$1\times10^{-5}\left[m^3\cdot mol^{-1}\right]$	–
$\tilde{L}^{\alpha\beta}$	interface mobility for solid phases	$1\times10^{-9}\left[m^3\cdot(J\cdot s)^{-1}\right]$	refs. [39,62]
M^{α}_{LiLi}	chemical mobility of Li	$2\times10^{-14}\left[mol^2\cdot(J\cdot m\cdot s)^{-1}\right]$	refs. [19,85]
$\kappa^{\alpha\beta}_{Li}$	dissipation rate	$\frac{4}{\Delta r}M^{\alpha}_{LiLi}$	–
κ^{se}_{Li}	electrode reaction rate	auto-change	ref. [25]
ω	relaxation factor	0.8	estimated

Ernzerh (PBE) [81] generalized gradient approximation. The cutoff energy for plane wave was set 520[eV], and only the Γ point was used for the Brillouin zone sampling. The energy and force convergence criterion for the lattice relaxation were set as 10^{-5}[eV] and $0.01\left[eV\cdot Å^{-1}\right]$, respectively. By randomly inserting or removing lithium atoms in the crystal cell of Li_xSn, and relaxing the cell to equilibrium, as shown in Fig. 3, the volume of crystals can be fitted as linear functions $\left[m^3/mol\right]$ with respect to field variable $x_{Li}^{Li_xSn}$

$$V_m^{Li_{0.4}Sn}\left(x_{Li}^{Li_{0.4}Sn}\right)=4.748\times10^{-6}\times\frac{x_{Li}^{Li_{0.4}Sn}}{1-x_{Li}^{Li_{0.4}Sn}}+1.855\times10^{-5}, \tag{29a}$$

$$V_m^{LiSn}\left(x_{Li}^{LiSn}\right)=3.073\times10^{-6}\times\frac{x_{Li}^{LiSn}}{1-x_{Li}^{LiSn}}+2.287\times10^{-5}, \tag{29b}$$

$$V_m^{Li_{2.6}Sn}\left(x_{Li}^{Li_{2.6}Sn}\right)=5.65\times10^{-6}\times\frac{x_{Li}^{Li_{2.6}Sn}}{1-x_{Li}^{Li_{2.6}Sn}}+2.489\times10^{-5}, \tag{29c}$$

$$V_m^{Li_{3.5}Sn}\left(x_{Li}^{Li_{3.5}Sn}\right)=4.781\times10^{-6}\times\frac{x_{Li}^{Li_{3.5}Sn}}{1-x_{Li}^{Li_{3.5}Sn}}+3.153\times10^{-5}. \tag{29d}$$

The volume functions will be used as the input parameter to Eq. (28). Since the elastic constants of all phases within the Li-Sn system have already been investigated by Zhang et al. [26], their data are used in the present simulation, which are listed in Table 1.

Thermodynamic energy density is also needed in this work. Several groups of researcher have studied the thermodynamic energy of the Li-Sn system by DFT calculations [25,26], experiments [20,22] and thermodynamic assessment [21,22]. Formation energies [26] of $Li_{0.4}Sn$, LiSn, $Li_{2.6}Sn$ and $Li_{3.5}Sn$ phases involved in simulation are listed in Table 2. These phases are stoichiometric compounds and their Gibbs free energy can be calculated by an equation of the form

$$G_m^{Li_xSn}=\left(xG_m^{BCC\_Li}+G_m^{BCT\_Sn}\right)/(x+1)+\Delta G_m^{Li_xSn}. \tag{30}$$

The composition ratios of all five phases (include pure Sn) are determined. From a realistic point of view, any stoichiometric compound also has a tiny amount of solid solution [82]. Based on this idea, the Gibbs free energies are treated by the numerical model, as presented in Appendix B. For stoichiometric compounds, during the simulation, the default values of the control parameters in the presented numerical model are $m=2$ and $x_{range}=0.1$ (homogeneity range), respectively.

The chemical potential of lithium can be solved by the bulk energy density and the diffusion potential of lithium

$$\mu_{Li}=V_m\left[f_{bulk}+(1\quad x_{Li})\tilde{\mu}_{Li}\right], \tag{31}$$

where molar fraction (x_{Li}) and diffusion potential of lithium ($\tilde{\mu}_{Li}$) are calculated by $x_{Li}=\sum_\alpha\phi_\alpha x_{Li}^\alpha$ and $\tilde{\mu}_{Li}=\sum_\alpha\phi_\alpha\tilde{\mu}_{Li}^\alpha$, respectively. Generally, the output voltage is calculated by the average chemical potential on the surface of the electrode. In this work, due to the nanoparticle with radius R is small enough, the average chemical potential ($\overline{\mu}_{Li}$) can also be obtained by integrating $\mu_{Li}(\boldsymbol{r})$ of the particle

$$\overline{\mu}_{Li}=\frac{3}{4\pi r^3}\int_{r=0}^{R}\mu_{Li}(\boldsymbol{r})4\pi r^2dr. \tag{32}$$

In addition, the average lithium concentration ($\overline{x}_{Li}$) can be calculated likewise.

And, as assumed above, another electrode of the full cell is pure Li, the chemical potential of lithium is μ_{Li}^{anode}. The operating voltage (V) of this full cell can be calculated by the following equation [84]

$$V=\frac{\overline{\mu}_{Li}-\mu_{Li}^{anode}}{\mathscr{F}}. \tag{33}$$

The other basic material parameters used in this work are summarized in Table 3. For the simulation of the Li_xSn system, some material parameters are determined by experiments and ab-initial calculations, while others that have little influence on the results are evaluated to ensure that the phase and phase-concentration fields evolve stably and efficiently. Among these parameters, the average molar volume (V_m, see eqs. (9, 10 and 18)) for solid phases is set as $1\times10^{-5}\left[m^3\cdot mol^{-1}\right]$. According to Refs. [19,85], the chemical mobility of lithium (M^{α}_{LiLi}, see Eq. (15)) in electrodes is set to be $2\times10^{-14}\left[mol^2\cdot(J\cdot m\cdot s)^{-1}\right]$. The radius of nanoparticle is set to be consistent with Courtney's work [25]. Specifically, the radius of the nanoparticle is about 5[μm] (as shown in Fig. 2), thus the edge length of the spatial grid Δr is set as 1×10^{-7}[m]. The applied current during cycling is a constant 37.2[mA/g] (about C/6 rate) [25]. Furthermore, considering the constraints of equal chemical potential at the interface, the dissipation rate ($\kappa^{\alpha\beta}_{Li}$, see Eq. (20)) is evaluated in Appendix A

$$\kappa^{\alpha\beta}_{Li}=\frac{4}{dr}M^{\alpha}_{LiLi}. \tag{34}$$

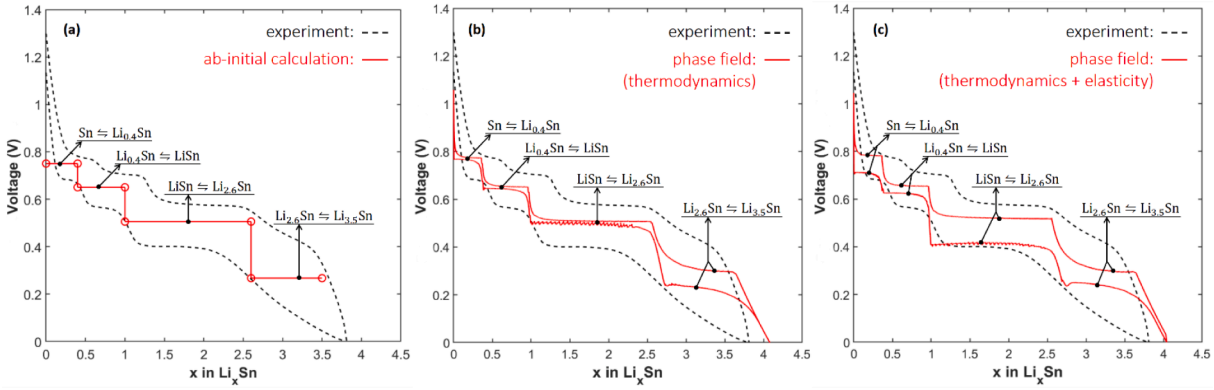

Fig. 4. (a-c) Result from experiment and DFT calculations (by Ref. [25]), and results from phase-field simulation under charging and discharging process, where the results of the phase-field simulation are the outcome of this work.

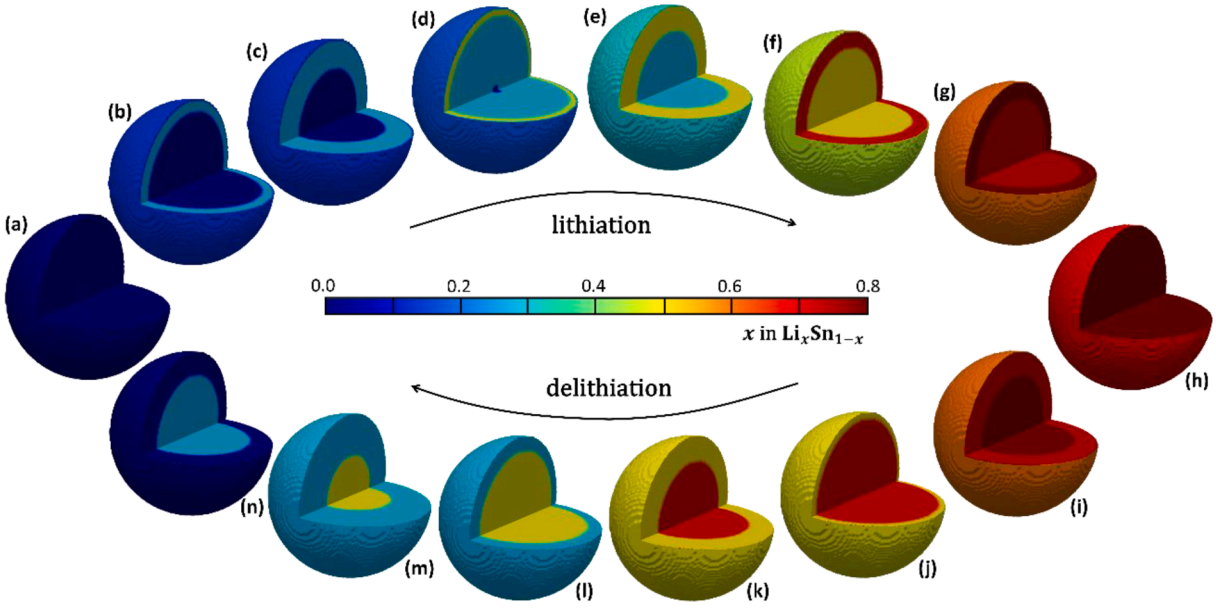

Fig. 5. The distribution of lithium concentration in nanoparticles during (de-)lithiation simulation, where simulation time (a) at 0th second; (b) at 1000th second; (c) at 3000th second; (d) at 5000th second; (e) at 7000th second; (f) at 10000th second; (g) at 13000th second; (h) at 14000th second; (i) at 15000th second; (j) at 16000th second; (k) at 18000th second; (l) at 21000th second; (m) at 23000th second; (n) at 26000th second.

Now, there are material parameters for diffusion and dissipation terms in phase-concentration equations. When the electrode reaction is slower, in order to enable the phase-concentration equations to evolve stably and efficiently $(\Delta x^{\alpha} \approx 10^{-3})$, the time interval Δt can be evaluated as 10^{-3}[s].

According to the principle of energy competition, the diffuse phase interface cannot be formed while the interface energy density $(\xi^{\alpha\beta}/\Delta \boldsymbol{r})$ is much smaller than the driving force $(\Delta^{\alpha\beta})$. To address this issue, Schoof et al. [86] presented a constructed interfacial energy $\xi^{\alpha\beta} = \widehat{\xi}^{\alpha\beta} + \xi^{*}$ in a strongly nonequilibrium system, where $\widehat{\xi}^{\alpha\beta}$ is the interfacial energy for the materials and ξ^{*} can be understood as a special energy with which a stable diffuse interface can be artificially constructed. In our work, the interfacial energy for Li_xSn phases $\widehat{\xi}^{\alpha\beta}$ is $0.1\,[\mathrm{J{\cdot}m^{-2}}]$ [27] and the value of ξ^{*} is chosen to be $9.9\,[\mathrm{J{\cdot}m^{-2}}]$. This means that the interfacial energy density is slightly lower than the thermodynamic driving force, so that the driving force and diffusion potential gradients at the phase interface approach equilibrium during the charge/discharge process at a slow electrode reaction rate. Assuming that the multiphase equations evolve stably and efficiently $(\Delta\phi^{\alpha} \approx 10^{-3})$, the interfacial mobility $L^{\sim\alpha\beta}$ (see Eq. (14)) is calculated as $10^{-9}\,[\mathrm{m^3{\cdot}(J{\cdot}s)^{-1}}]$.

Moreover, it should be taken into account that the emergence of new phases and the disappearance of old ones dynamically increase $\partial_t \phi^{\alpha}$, which also affects the stability of the phase-concentration evolvement. The equation $\Delta\widehat{t} = \Delta t \times \Delta^{*}$ is introduced to control the variation of the time interval (as shown in Appendix C), where Δt is the evaluated time interval and Δ^{*} can be understood as a factor to scale the time interval. In general, Δ^{*} can be calculated by the formula $\Delta^{*} = \min\left(10^{-3}/|\Delta\phi^{\alpha}|^{max}, 10^{-3}/|\Delta x^{\alpha}|^{max}\right)$, at each simulation step, where $|A|^{max}$ denotes the maximum absolute value of A in the domain. The default value of the relaxation factor (ω, in Eq. (28)) is set to 0.8. The interface width (ε, in Eq. (3)) is set to be $4 \times \boldsymbol{dr}$ (as discussed in Appendix A).

The present results are compared with the experimental and DFT-calculated results of Courtney et al. [25]. Thus, the charge/discharge rates are set to be consistent with their work. Specifically, the current applied during the cycle is a constant 37.2[mA/g] (an approximate rate of C/6), which can be converted into the amount of change in lithium concentration per unit time $\Delta\bar{x}_{\mathrm{Li}}/\Delta t \overset{\mathrm{def}}{=} 4.5764 \times 10^{-5}\,[\mathrm{s}^{-1}]$. Therefore,

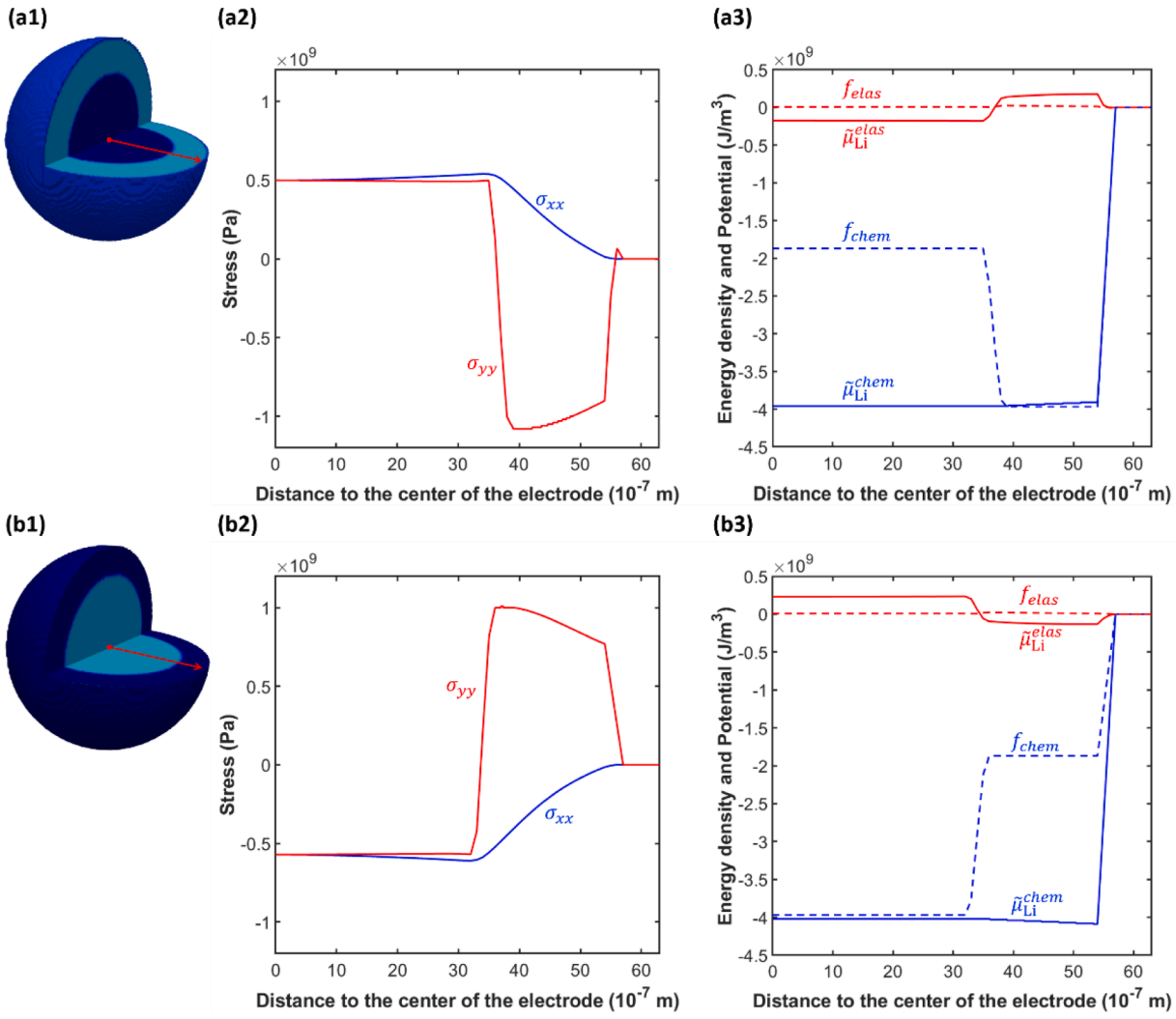

Fig. 6. Stress, energy density and diffusion potential distribution in nanoparticle at (a1-a3) 1000th second and (b1-b3) 26000th second.

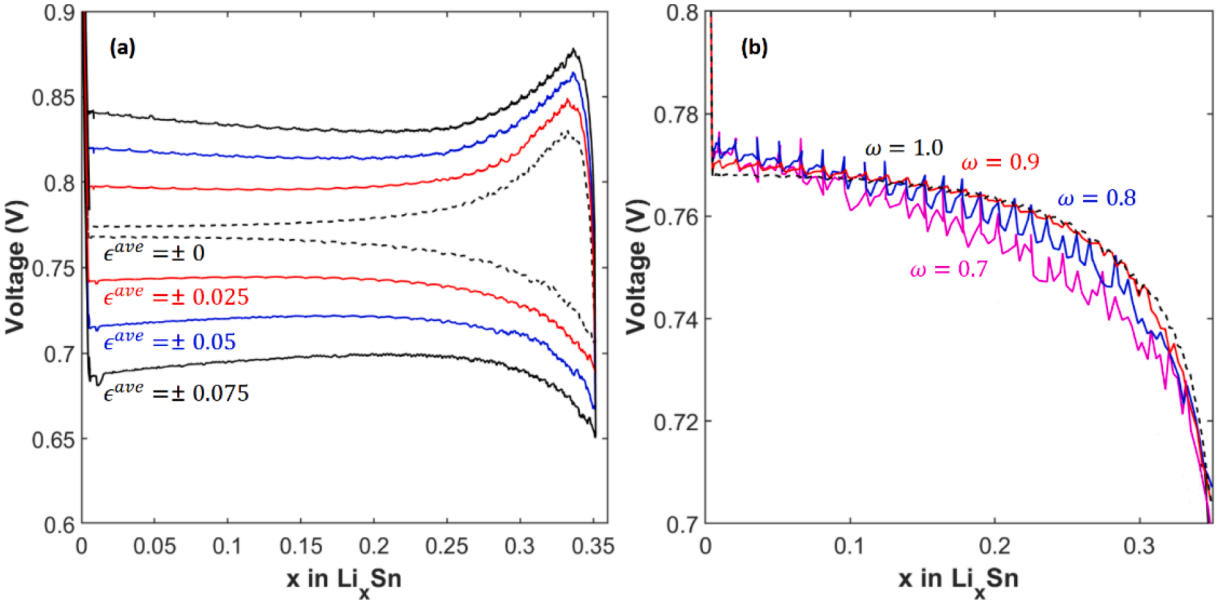

Fig. 7. Effect of the (a) the averaged eigenstrain (ϵ^{ave}) and (b) the relaxation factor (ω) on the voltage profile during the lithiation/delithiation cycle of Sn-$Li_{0.4}$Sn two-phase.

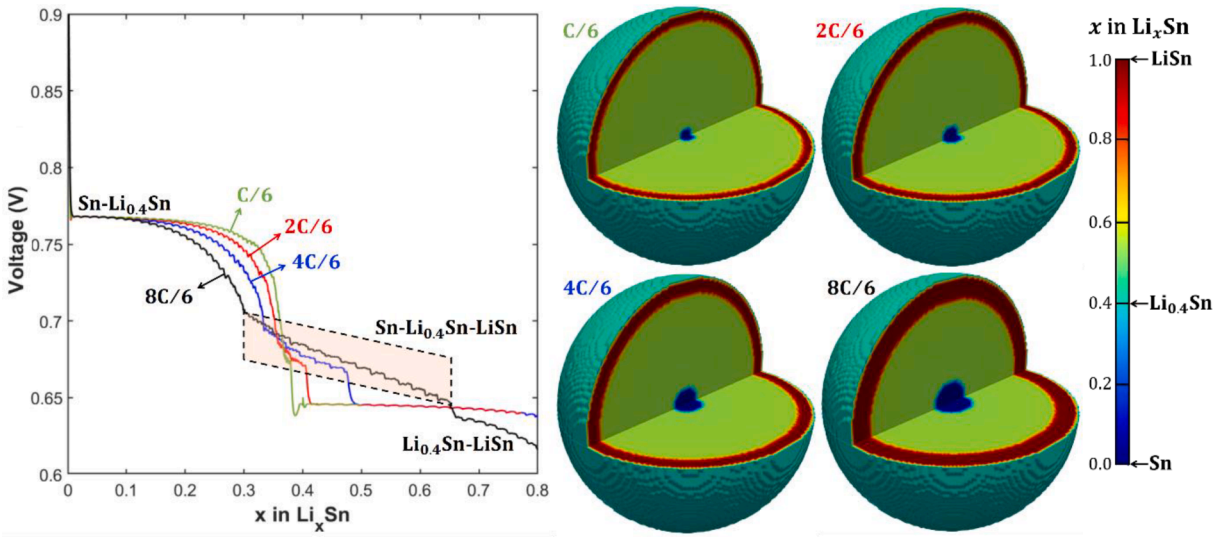

Fig. 8. Effect of the electrode reaction rate during discharging process in the present of Sn-Li$_{0.4}$Sn-LiSn three-phase coexistence. The voltage profiles are calculated with varying C-rate, and the voltage curves for the three-phase coexistence are indicated by a dashed parallelogram. The diagrams on the left show the concentration distribution in the case of three-phase coexistence.

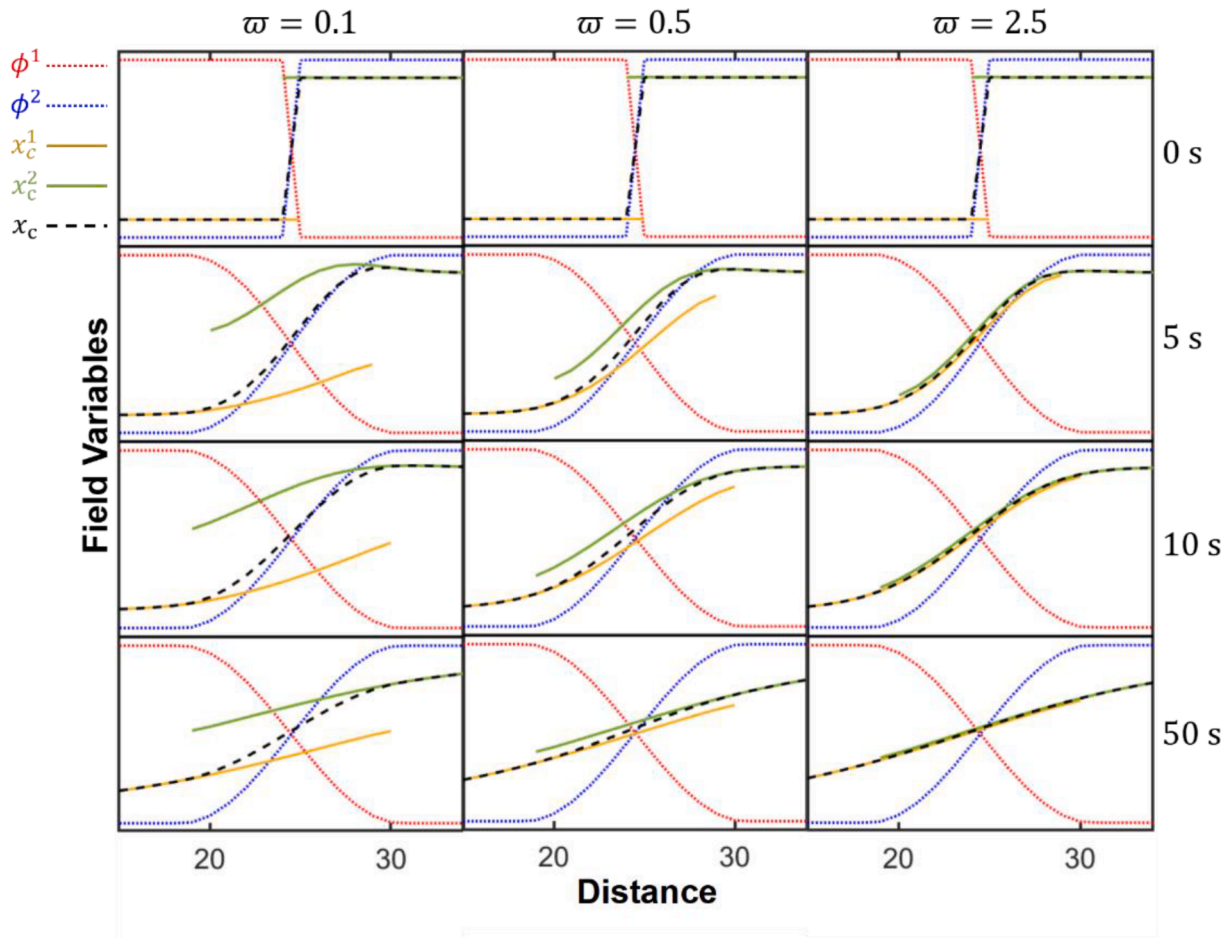

Fig. A1. Distribution of field variables (ϕ^1, ϕ^2, x_c^1, x_c^2 and x_c) at the interface during simulation, where the columns represent the use of different ϖ values and the rows represent different times.

the average lithium concentration $\overline{x}_{\mathrm{Li}}$ in the nanoparticles is periodically calculated with Eq. (C.1). If $\Delta\overline{x}_{\mathrm{Li}}/\Delta t$ is larger than the defined value, the rate of the electrode reaction ($\kappa_{\mathrm{Li}}^{se}$, see Eq. (21)) is set smaller, otherwise, $\kappa_{\mathrm{Li}}^{se}$ is set larger (as shown in Appendix C).

4. Results

The multiphase-multicomponent phase-field model can be verified by experiment and DFT calculations in Ref. [25]. To describe the

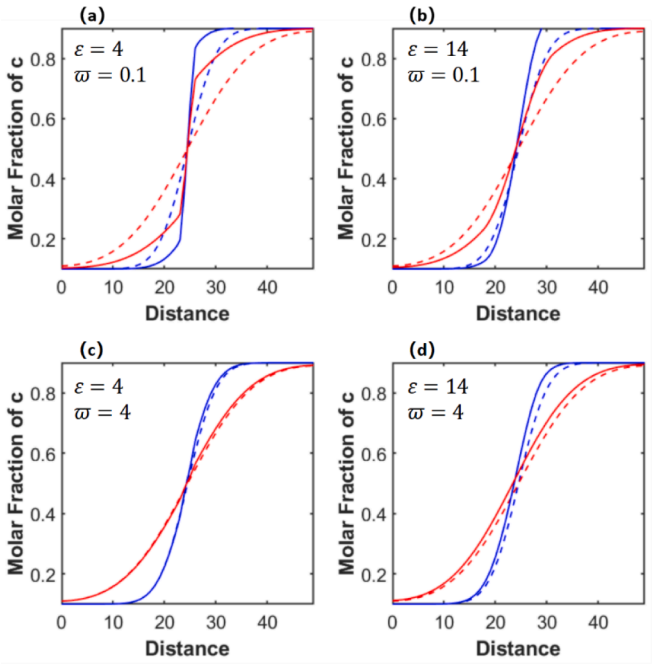

Fig. A2. The effects of interface width and dissipation rate on the evolution of phase-concentration field are investigated by comparing the calculated results of the phase-concentration (solid curves) and the mass-conservation (dashed curves) equations.

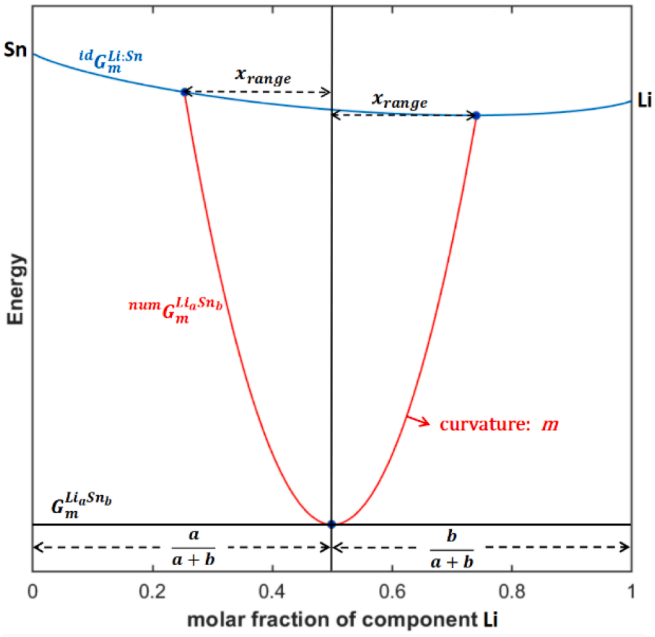

Fig. B1. Schematic diagram of the energy curve for numerical model.

nanoparticle size and morphology, the charging/discharging rate and the diffusion coefficient of lithium are set the same as the experiment values. The voltage profiles computed by the present simulation agree well with those measured by Courtney et al. [25]. The voltage plateau obtained from DFT calculations can be used to predict the tendency of the experimental voltage profile, as indicated in Fig. 4(a). Since this method is based on the balance of energy to estimate the open-circuit voltage, the obtained voltage curve is like a ladder, which gives no difference in the results obtained between charging and discharging process for battery. On the contrary, the present simulation can predict

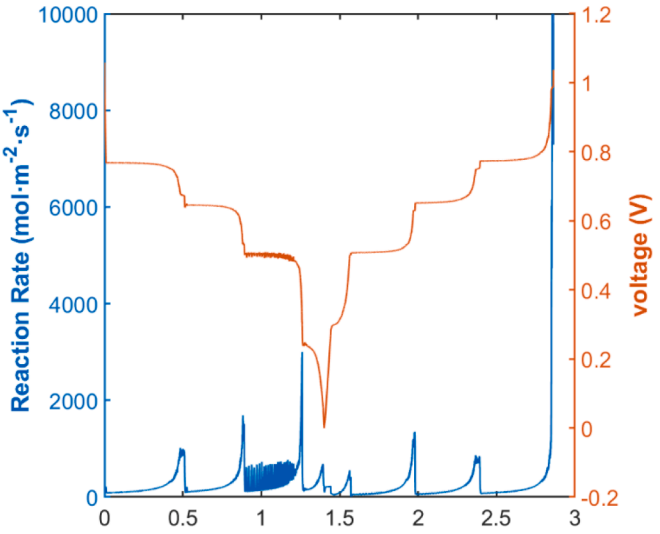

Fig. C1. Variation of electrode reaction rate and voltage with respect to real time.

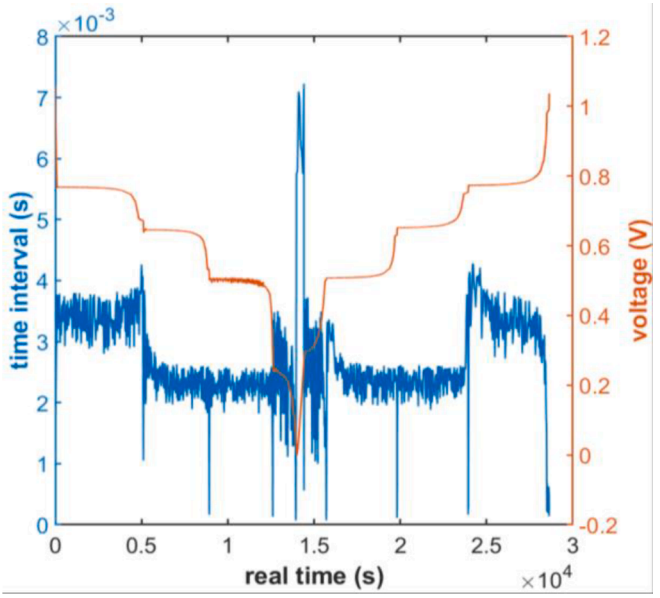

Fig. C2. Variation of time interval and voltage with respect to real time.

the voltage profiles for both charging/discharging, as shown in Fig. 4(b). And as presented in Fig. 4(c), it is possible to combine thermodynamic energy and elastic energy to simulate the hysteresis of voltage due to elasticity, which has been demonstrated by many works [87–89].

Fig. 5 is the distribution of lithium concentration in nanoparticles during (de-)lithiation simulation. Both pure Sn, $Li_{0.4}Sn$, LiSn, $Li_{2.6}Sn$ and $Li_{3.5}Sn$ phases have limited homogeneity ranges[22], which are also illustrated in Fig. 5(a-n), where the lithium concentration has a sudden jump at the interface. It illustrates that the simulation starts with the insertion of lithium atoms into the surface of nanoparticle, and then the diffusion potential of lithium and the energy density on surface rise rapidly. Such a rise leads to the transformation of the lattice structure from Sn phase into the $Li_{0.4}Sn$ phase. The lithium concentration profiles at the 1000th and 3000th seconds show that lithium diffuses toward the center of the nanoparticle, followed by the continuous growth of the $Li_{0.4}Sn$ phase. It corresponds to the first voltage plateau of the relatively lower red curve, as shown in Fig. 4(b and c). When the discharging process proceeds to the 5000th second, the LiSn phase is generated on

the nanoparticle surface, indicating that the voltage profile reaches the start of the second plateau. Then the LiSn phase is growing and the Sn phase is disappearing. At 7000th second, the LiSn phase is coexisting with the $Li_{0.4}Sn$ phase. Similarly, at 10000th second, the $Li_{0.4}Sn$ phase disappears, the $Li_{2.6}Sn$ phase is coexisting with the LiSn phase, and the voltage of nanoparticle comes to the third plateau. The last generated phase is $Li_{3.5}Sn$ at about 13000th second. In the experimental results of this stage, we can observe a tendency to form a voltage plateau, but in fact it does not succeed. The same results were also obtained by Lopez et al. [4] and Zhou et al. [14], especially in the work of Lopez et al., where all voltage plateaus have a large tilt angle during the whole charge/discharge cycle. How the tilt angle is generated is discussed in Sections 5.2 and 5.3.

Then, in this simulation, the discharging process automatically switches to the charging process. When the chemical potential of lithium in nanoparticle is equal to that of pure Li, i.e., the operating voltage is 0[V] at around 14000th second. The voltage profile of the charging process is the relatively upper red curve, as indicated in Fig. 4(b and c), which is the opposite of the discharging process. When the delithiation process continues, the concentration of lithium on the surface of nanoparticle decreases, and it results in the generation of the lithium-poor phase. When the charging process proceeds to around 27000th second, only Sn phase remains in the nanoparticle, which means that one cycle of charging/discharging process of cell is finished.

5. Discussion

5.1. *Elasticity in* $\mathbf{Li_xSn}$ *nanoparticle*

Fig. 6 shows the distribution of stress, energy density and diffusion potential of lithium within the nanoparticle corresponding to the 1000th and the 26000th seconds of the lithiation/delithiation cycle indicated in Fig. 5. Generally, there are two phases coexisting in the nanoparticle. For the nanoparticle at 1000th second, the outer phase is lithium-rich and the inner phase is lithium-poor. For the nanoparticle at 26000th second, the outer phase is lithium-poor and the inner phase is lithium-rich.

When the outer phase of the particle is lithium-rich (e.g., Fig. 6a1–a3), the radial stress (σ_{xx}) of the particle is hydrostatic tension, and the hoop stress (σ_{yy}) exhibits as hydrostatic compression in the lithium-rich region and hydrostatic tension in the lithium-poor region. This is the same as the existing purely elastic calculations [90]. Comparing the distribution of chemical and elastic energy densities and potentials within the particles, the chemical energy density (f_{chem}) and elastic diffusion potential ($\mu^{\sim elas}_{\mathrm{Li}}$) have a large jump at the phase interface, while the elastic energy density (f_{elas}) and chemical diffusion potential ($\mu^{\sim chem}_{\mathrm{Li}}$) have little effect on the total energy and potential due to the small amount of lithium insertion. As the lithiation reaction proceeds, the lithium-poor phase is continuously transformed into the lithium-rich phase by the driving force consisting of energy density and potential (eqs. (9, 10)). In this process, the elastic diffusion potential of lithium in the surface of the nanoparticle is higher than that in the center, which is consistent with the theory that elasticity provides an important part of the lithium diffusion driving force in electrode [35,36].

When the outer phase of the particle is lithium-poor (e.g., Fig. 6b1–b3), the curve trends for the stress, the energy density and the diffusion potential are opposite to the process of lithiation reaction. The radial stress of the particle is hydrostatic compression, and the hoop stress exhibits as hydrostatic tension in the lithium-rich region and hydrostatic compression in the lithium-poor region. The chemical energy density is higher in the surface and the elastic diffusion potential is higher in the core of the nanoparticle. However, the elasticity plays the same role as the lithiation process that in promoting the diffusion of lithium in the delithiation reaction process.

5.2. *Eigenstrain in* $\mathbf{Li_xSn}$ *nanoparticle*

Eq. (23) is the phase eigenstrain model for Li_xSn, which makes it possible to use the elastic parameters obtained from DFT calculations in the phase-field simulation. There are two parameters in phase eigenstrain model (ϵ^{ave} and ω) that can be estimated.

As shown in Fig. 7(a), in order to save computational effort, a lithiation/delithiation cycle for Sn-$Li_{0.4}Sn$ two-phase is established. The voltage curves of the black dashed, red solid, blue solid, and black solid lines correspond to simulations in which the average strains are taken as ±0, ±0.025, ±0.05, and ±0.075, respectively. During the lithiation process, the nanoparticle is expanded and the average lattice strain is set positive. In contrast, the nanoparticle is contracted and the average lattice strain is set negative during the delithiation process. It can be seen that while the absolute average eigenstrain increases, the difference between the voltage curves of the lithiation and the delithiation also increases. This result is similar to those reported by Lu et al. [87], Jin et al. [88] and Bucci et al. [89]. The pressure causes a hysteresis in the voltage profile, which can separate the charging and discharging voltage curves.

In Fig. 7(b), voltage curves during lithiation process of Sn-$Li_{0.4}Sn$ phases with different ω values are shown. The relaxation factor ω was adjusted to 1.0, 0.9, 0.8, and 0.7 to obtain voltage profiles in black dashed, red solid, blue solid, and purple solid formats, respectively. The smaller value of the ω, the greater the elastic/structural inhomogeneity within the nanoparticle. Besides, it indicates that the increased inhomogeneity of eigenstrain leads to a more inhomogeneous elastic strain and stress, which would result in a larger gap in the diffusion potential and the energy density at the two-phase interface and finally responds to a stronger oscillation of the voltage profile. And it can be observed that the voltage curve becomes more skewed as the elastic/structural inhomogeneity rises. This phenomenon according to the present simulation is found in the experimental voltage profiles on sn-based electrode materials by Lopez et al. [4], Beaulieu et al. [15] and Mukhopadhyay et al. [8].

5.3. *Three-phase coexistence in* $\mathbf{Li_xSn}$ *nanoparticle*

The tilt of the voltage plateau is not only caused by the elastic/structural inhomogeneity, but also affected by the phase inhomogeneity, such as co-existence of multiple phases. When the discharge current (controlled by $\kappa^{se}_{\mathrm{Li}}$) increases, three-phase coexistence within the nanoparticle occurs due to the limitations of the chemical mobility for lithium and the size of the particle. As demonstrated in Fig. 8, the discharge current of the simulation, whose voltage curve is drawn in green color, is set to 37.2[mA/g] (about C/6 rate). The red, blue, and black curves refer to the voltage profile for twice, four and eight times the discharge current of the green curve, respectively. The increase of discharge current decreases the percentage of the voltage plateau in the voltage curve. In replacement is a sloping voltage curve, which represents the coexistence of the three phases (Sn-$Li_{0.4}Sn$-LiSn) in nanoparticle currently. It means that the output voltage of the battery becomes more unstable. In addition, the distribution of lithium concentration in nanoparticle shows that the region of three-phase coexistence is extended while the discharge current increases. This is because the diffusion of lithium in the nanoparticles is nearly balanceed at a slow electrode reaction rate (C/6 rate). As the rate of the electrode reaction increases, limited by the diffusion/dissipation rate of the lithium, the diffusion potential gradient near the surface of the nanoparticle becomes larger. Therefore, phase transitions are more likely to occur near the particle surface and the third phase is more likely to grow. The more lithium is trapped by the third phase, the slower the phase in the center of the nanoparticle disappears. Finally, the region in which the three phases coexist is extended.

Therefore, this result proves that when the size of the nanoparticle is larger, the diffusion path of lithium from surface to the center of

electrode is longer, which increases the probability of multiphase coexistence. Increasing the discharge rate may furthermore promote the inhomogeneity of phase and component distribution in the electrode. This explains that nanosizing of the electrode, or usage of materials with the faster lithium diffusion rate can result in a battery with better and more stable electrochemical performance at high rates [6].

6. Conclusions

The coupling database is trending in performing electrode material design and numerical simulations. In this paper, we report a multiphase and phase-concentration modeling framework to calculate the voltage profile of electrode material by coupling its thermodynamic, kinetic, and elastic databases (from DFT and phase-diagram calculations). Within the framework of this model, the multiphase and the phase-concentration equations are integrated. The parameters in database for stoichiometric compounds (Li_xSn) are transformed into energy densities and diffusion potential to drive the phase transition and the component migration by numerical Gibbs free energy model and phase eigenstrain model. The simulation results are validated by voltage profile obtained from experiment [4,8,15,25].

Based on the developed models, the effect of the eigenstrain distribution and phase transition on the cells' output voltage is investigated. The expansion and contraction of the nanoelectrode particles during cell operation is one of the affecting factors leading to the separation of the lithiation and the delithiation voltage curves. The differences of molar volume of stoichiometric compounds lead to elastic/structural inhomogeneity within the nanoparticle, which causes the cell's output voltage unstable. For increasing discharge current to speed up the charging/discharging rate, the co-existence of three or more phases is more likely to be observed in the nanoparticle. It is also not beneficial for batteries to output voltage stably.

The results provide an insightful and useful modeling tool to describe the multiphase transition in electrode materials on the basis of material database, which can be used to guide the electrode material design by numerical simulations in future.

CRediT authorship contribution statement

Qi Huang: Methodology, Conceptualization, Software, Investigation, Formal analysis, Visualization, Validation, Writing - original draft, Writing - review & editing. **Simon Daubner:** Methodology, Conceptualization, Writing - review & editing. **Shiwei Zhang:** Methodology, Data curation, Writing - original draft. **Daniel Schneider:** Methodology, Conceptualization, Writing - review & editing. **Britta Nestler:** Methodology, Writing - review & editing. **Hong Mao:** Writing - review & editing. **Shuhong Liu:** Data curation. **Yong Du:** Methodology, Supervision, Project administration, Funding acquisition, Writing - review & editing.

Declaration of Competing Interest

The authors declare that they have no known competing financial interests or personal relationships that could have appeared to influence the work reported in this paper.

Data availability

Data will be made available on request.

Acknowledgments

Qi Huang wants to thank Geng Zhang, Yinping Zeng, Yuhui Zhang and Shiyi Wen for some discussions in phase fields, thermodynamics and kinetics. This work was supported by the Sino-German Cooperation Group GZ1528 'Integrated Computational Materials Engineering of Electrochemical Storage Systems', which is within the Nation Natural Science Foundation of China and Deutsche Forschungsgemeinschaft of Germany, and the National Natural Science Foundation of China (Grant Numbers: 52201010). Qi Huang is grateful for the scholarship from China Scholarship Council, which supports his research work in KIT, Germany from March 15th, 2022 to September 14th, 2023.

Part of the model formulation was funded by the Deutsche Forschungsgemeinschaft (DFG, German Research Foundation), under project ID 390874152, POLiS Cluster of Excellence (grant number: UP 33/1). This work contributes to the research performed at CELEST (Center for Electrochemical Energy Storage Ulm-Karlsruhe).

Contributions are also provided through the "Materials Science and Engineering (MSE)" Programme, no 43.31.01 supported by the Helmholtz assozciation which is gratefully acknowledged.

Appendix A

Evolution of multiphase and phase-concentration equations in one dimension

First, we need to build a simple initial structure in alloys. The existence of phases 1 and 2 in the simulation domain is considered, and component c is present in both phases. Assuming that the properties of these two phases are same, the diffusion/dissipation driving forces (diffusion potential) can be simplified as the concentration gradient. Then, considering that there are no other chemical reactions in two phases, the phase-concentration equations for phases 1 and 2 can be simplified as follows:

$$\phi^1\frac{\partial x_c^1}{\partial t} = \nabla\cdot\left(\phi^1 M_{cc}\nabla x_c^1\right) + \left|\nabla\phi^{12}\right|\kappa_c^{12}\left(x_c^2 \quad x_c^1\right) \quad x_c^1\frac{\partial\phi^1}{\partial t}, \tag{A1}$$

$$\phi^2\frac{\partial x_c^2}{\partial t} = \nabla\cdot\left(\phi^2 M_{cc}\nabla x_c^2\right) + \left|\nabla\phi^{21}\right|\kappa_c^{21}\left(x_c^1 \quad x_c^2\right) \quad x_c^2\frac{\partial\phi^2}{\partial t}, \tag{A2}$$

where M_{cc} is the chemical mobility of component c in two phases, $\left|\nabla\phi^{12}\right|$ is equal to $\left|\nabla\phi^{21}\right|$ and κ_c^{12} is equal to κ_c^{21}. In general, in alloys, the diffusion rate of substances on grain boundaries is slightly higher than that within the bulk. So, we assume that the diffusive term is equal to the dissipation term in Eq. (A.1) and replace all the dimensionless variables with parameter ϖ. The following relationship between M_{cc} and κ_c^{12} can be obtained

$$\kappa_c^{12} = \frac{\varpi/(d\boldsymbol{r})^2}{1/d\boldsymbol{r}}M_{cc} = \frac{\varpi}{d\boldsymbol{r}}M_{cc}. \tag{A3}$$

The discussion will undoubtedly be complicated if the effect of the phase transition on the evolution of the phase concentration is considered. We assume that there is no driving force between phases 1 and 2, set $d\boldsymbol{r}$ to 1.0 and dt to 1×10^{-3}[s]. The left side of the domain is filled with phase 1 and its

x_c^1 is 0.1. The right side of the domain is filled with phase 2 and its x_c^2 is 0.9. The interface width ε is set to 14. M_{cc} is set to 1. Besides, the parameter ϖ is set to 0.1, 0.5 and 2.5 to demonstrate the effect of dissipation rate κ_c^{12}. The simulation results are shown in Fig. A1, where the red dot curve is ϕ^1, the blue dot curve ϕ^2, the yellow solid curve x_c^1, the green solid curve x_c^2 and the black dashed curve x_c (computed by $x_c = \phi^1 x_c^1 + \phi^2 x_c^2$).

In Fig. A.1, the diffuse interface is formed within 5 s. The bigger the value of ϖ, the smaller the distribution of concentration is affected by the interface formation and the better the curve of phase-dependent concentration is fitted to the curve of concentration as well. Considering the physical relationship between dissipation and diffusion in alloys and the numerical performance here, it is more appropriate to take $\varpi \geq 2.5$ in simulation.

The evolution of the phase-concentration equation is compared with the results of mass-conservation equation to verify its validity. The initial component distribution is the same as in the work above. And the simplified mass-conservation equation is

$$\frac{\partial x_c}{\partial t} = \nabla \cdot M_{cc} \nabla x_c, \tag{A4}$$

where M_{cc} is the chemical mobility of component c in simulation domain. It is set to be the same as the diffusion rate in the phase-concentration equation.

As shown in Fig. A.2, the parameter $\{x_c\}$, which is computed by phase-concentration equations, is compared with the same parameter $[x_c]$ evolved by the mass-conservation equation. The dashed and solid curves are the distribution of $[x_c]$ and $\{x_c\}$, respectively. The blue and red curves (both in solid and dashed format) are the results at 10th second and 50th second, respectively. The grain boundary width and dissipation rate were changed in four simulations, where ε was set as 14 and 4, and ϖ as 0.1 and 4. The diffusion rate (M_{cc}) is set as a constant in mass-conservation and phase-concentration equations. Therefore, as indicated by the dashed line in Fig. A.2, the distributions of $[x_c]$ are same in all four simulations. The solid-line results $\{x_c\}$ are different with each other. As demonstrated in Fig. A.2(a, b), the parameter ϖ is set as 0.1. $\{x_c\}$ deviates significantly from $[x_c]$ at the interface. As shown in Fig. A.2(c, d), the parameter ϖ is set as 4. The distribution of $\{x_c\}$ is more like $[x_c]$. And when the interface is set relatively narrow ($\varepsilon = 4$), the results of phase-concentration equations and the mass-conservation equation are almost the same. Therefore, the width of the interface in present work is set as $4 \times dr$ and ϖ is set as 4.

Appendix B. Numerical model of Gibbs free energy for Li_xSn phase

As shown in Fig. B.1, in order to incorporate the effect of component concentration in the Gibbs free energy for the stoichiometric compound and to give it a certain solubility, the following numerical model of Gibbs free energy is proposed

$$^{num}G_m^{Li_aSn_b}(x_{Li}, x_{Sn}, T) = (1 \quad n_{scale}(x_{\mathrm{Li}}, x_{\mathrm{Sn}}))G_m^{\mathrm{Li}_a\mathrm{Sn}_b}(T) + n_{scale}(x_{\mathrm{Li}}, x_{\mathrm{Sn}})\,{}^{id}G_m^{Li:Sn}(x_{Li}, x_{Sn}, T), \tag{B1}$$

where $G_m^{\mathrm{Li}_a\mathrm{Sn}_b}(T)$ is the Gibbs free energy of $\mathrm{Li}_a\mathrm{Sn}_b$, which can be calculated by Eq. (25). $n_{scale}(x_{\mathrm{Li}}, x_{\mathrm{Sn}})$ is the relaxation function between the Gibbs free energy of $\mathrm{Li}_a\mathrm{Sn}_b$ to the ideal mixing energy of Li and Sn, which is defined as

$$n_{scale}(x_{\mathrm{Li}}, x_{\mathrm{Sn}}) = \frac{1}{2}\left\{\left[\frac{|x_{\mathrm{Li}} \quad a/(a+b)|}{x_{range}}\right]^m + \left[\frac{|x_{\mathrm{Sn}} \quad b/(a+b)|}{x_{range}}\right]^m\right\}, \; m > 0 \tag{B2}$$

where m controls the curvature of the energy curve of the numerical model, x_{range} determines the solubility of the stoichiometric compound. And the function ${}^{id}G_m^{\mathrm{Li:Sn}}(x_{\mathrm{Li}}, x_{\mathrm{Sn}}, T)$ in Eq. (B.1) is ideal mixing energy of Li and Sn, which is written as

$${}^{id}G_m^{\mathrm{Li:Sn}}(x_{\mathrm{Li}}, x_{\mathrm{Sn}}, T) = x_{\mathrm{Li}}G_m^{\mathrm{Li}}(T) + x_{\mathrm{Sn}}G_m^{\mathrm{Sn}}(T) + RT[x_{\mathrm{Li}}\ln(x_{\mathrm{Li}}) + x_{\mathrm{Sn}}\ln(x_{\mathrm{Sn}})], \tag{B3}$$

where $G_m^{\mathrm{Li}}(T)$ and $G_m^{\mathrm{Sn}}(T)$ are the energies of the reference states of Li and Sn, respectively. In the present work, Li with the crystal structure of BCC and Sn with the crystal structure of BCT are chosen as the reference states.

Appendix C. Automatic adjustment of time interval and electrode reaction rate

In this work, to ensure the accuracy and numerical stability of the simulation, two important parameters are automatically adjusted by the program, namely time interval and electrode reaction rate.

The blue curve shown in Fig. C.1 displays the variation of the electrode reaction rate during one cycle. And the orange curve is the voltage curve. The electrode reaction rate ($\kappa_{\mathrm{Li}}^{se}$, see Eq. (21)) establishes a peak at the beginning of each voltage plateau which rapidly drops to a stable value after that. It is caused by the systematic lithium loss which exists when a 3D simulation is reduced to 1D or 2D simulation. Since the average lithium concentration $\bar{x}_{\mathrm{Li}}$ can be derived from the lithium concentration $x_{\mathrm{Li}}(\boldsymbol{r})$ distributed on the nanoparticle radius by

$$\bar{x}_{\mathrm{Li}} = \frac{3}{4\pi r^3}\int_{r=0}^{R} x_{\mathrm{Li}}(\boldsymbol{r}) 4\pi r^2 dr. \tag{C1}$$

When lithium diffuses in the 1D simulation domain, the average lithium concentration calculated for 3D nanoparticle is automatically reduced (or increase during delithiation process). To define a boundary condition so that a constant current of 37.2[mA/g] (about C/6 rate) is imposed, the electrode reaction rate $\kappa_{\mathrm{Li}}^{se}$ needs to be automatically adjusted as shown in the Fig. C.1.

However, it is important to note that this is a numerical method to compensate for systemic lithium losses. This method is feasible for small nanoparticles as in the considered simulations, which have defects for larger size electrode particles.

The blue and the orange curves (shown in Fig. C.2) illustrate the variation of the time interval and voltage during one cycle. The time interval decreases automatically when a new phase is generated or a previously formed phase disappears. The evolution of the phase volume fraction will be transiently decelerated to reduce the impact on the evolution of the phase concentration (illustrated in Fig. A.1). This process ensures that the local

lithium concentration is normal and the results of voltage profiles are physically founded.

Therefore, the amount of phase volume fraction variation at each time step is limited in the program. If the phase volume fraction performs substantial local changes, the time interval automatically reduces. This procedure makes the phase-concentration field evolve more stable. It can avoid the computational waste due to the slow evolution of field variables.

References

[1] R.A. Huggins, J. Power Sources 81 (1999) 13–19, https://doi.org/10.1016/S0378-7753(99)00124-X.

[2] M. Winter, J.O. Besenhard, Electrochim. Acta 45 (1999) 31–50, https://doi.org/10.1016/S0013-4686(99)00191-7.

[3] Y. Zou, Y. Wang, ACS Nano 5 (2011) 8108–8114, https://doi.org/10.1021/nn2027159.

[4] J.L.L. Lopez, P.J. Grandinetti, J. Mater. Chem. A 7 (2019) 10781–10794, https://doi.org/10.1039/C9TA03345A.

[5] K. Ui, S. Kikuchi, Y. Kadoma, N. Kumagai, S. Ito, J. Power Sources 189 (2009) 224–229, https://doi.org/10.1016/j.jpowsour.2008.09.081.

[6] Y.-M. Chiang, Science, 330 (2010) 1485-1486. 10.1126/science.1198591 10.1126/science.1198591.

[7] H. Tavassol, M.W. Cason, R.G. Nuzzo, A.A. Gewirth, Adv. Energy Mater. 5 (2015) 1400317, https://doi.org/10.1002/aenm.201400317.

[8] A. Mukhopadhyay, R. Kali, S. Badjate, A. Tokranov, B.W. Sheldon, Scr. Mater. 92 (2014) 47–50, https://doi.org/10.1016/j.scriptamat.2014.08.011.

[9] Y. Lu, Y. Ni, Mech. Mater. 91 (2015) 372–381, https://doi.org/10.1016/j.mechmat.2015.03.010.

[10] T. Danner, G. Zhu, A.F. Hofmann, A. Latz, Electrochim. Acta 184 (2015) 124–133, https://doi.org/10.1016/j.electacta.2015.09.143.

[11] C.V. Di Leo, E. Rejovitzky, L. Anand, Int. J. Solids Struct. 67 (2015) 283–296, https://doi.org/10.1016/j.ijsolstr.2015.04.028.

[12] J. Hou, S. Qu, M. Yang, J. Zhang, J. Power Sources 450 (2020), 227697, https://doi.org/10.1016/j.jpowsour.2019.227697.

[13] X. Wang, F. Fan, J. Wang, H. Wang, S. Tao, A. Yang, Y. Liu, H. Beng Chew, S. X. Mao, T. Zhu, Nat. Commun. 6 (2015) 1–7, https://doi.org/10.1038/ncomms9417.

[14] X. Zhou, T. Li, Y. Cui, Y. Fu, Y. Liu, L. Zhu, ACS Appl. Mater. Interfaces 11 (2019) 1733–1738, https://doi.org/10.1021/acsami.8b13981.

[15] L. Beaulieu, S. Beattie, T. Hatchard, J. Dahn, J. Electrochem. Soc. 150 (2003) A419, https://doi.org/10.1149/1.1556595.

[16] K.J. Rhodes, R. Meisner, M. Kirkham, N. Dudney, C. Daniel, Journal of The Electrochemical Society, 159 (2012) A294. Web. doi:10.1149/2.077203jes.

[17] J. Wang, D.X. Liu, M. Canova, R.G. Downing, L.R. Cao, A.C. Co, J. Radioanal. Nucl. Chem. 301 (2014) 277–284, https://doi.org/10.1007/s10967-014-3102-5.

[18] D.X. Liu, J. Wang, K. Pan, J. Qiu, M. Canova, L.R. Cao, A.C. Co, Angew. Chem. 126 (2014) 9652–9656, https://doi.org/10.1002/ange.201404197.

[19] C.-H. Chen, E. Chason, P.R. Guduru, J. Electrochem. Soc. 164 (2017) E3661, https://doi.org/10.1149/2.0661711jes.

[20] C.J. Wen, R.A. Huggins, J. Electrochem. Soc. 128 (1981) 1181. https://ui.adsabs.harvard.edu/link_gateway/1981JElS.128.1181W/doi:10.1149/1.2127590.

[21] F. Yin, X. Su, Z. Li, J. Wang, J. Alloy. Compd. 393 (2005) 105–108, https://doi.org/10.1016/j.jallcom.2004.09.047.

[22] D. Li, S. Fürtauer, H. Flandorfer, D.M. Cupid, Calphad 47 (2014) 181–195, https://doi.org/10.1016/j.calphad.2014.09.002.

[23] I.A. Courtney, J. Dahn, J. Electrochem. Soc. 144 (1997) 2045, https://doi.org/10.1149/1.1837740.

[24] S.-C. Chao, Y.-F. Song, C.-C. Wang, H.-S. Sheu, H.-C. Wu, N.-L. Wu, J. Phys. Chem. C 115 (2011) 22040–22047, https://doi.org/10.1021/jp206829q.

[25] I.A. Courtney, J. Tse, O. Mao, J. Hafner, J.R. Dahn, Phys. Rev. B 58 (1998) 15583, https://doi.org/10.1103/PhysRevB.58.15583.

[26] F. Zhang, J. Wang, S. Liu, Y. Du, J. Power Sources 330 (2016) 111–119, https://doi.org/10.1016/j.jpowsour.2016.08.136.

[27] K. Hirai, T. Ichitsubo, T. Uda, A. Miyazaki, S. Yagi, E. Matsubara, Acta Mater. 56 (2008) 1539–1545, https://doi.org/10.1016/j.actamat.2007.12.002.

[28] T. Li, H. Kang, X. Zhou, C. Lim, B. Yan, V. De Andrade, F. De Carlo, L. Zhu, ACS Appl. Mater. Interfaces 10 (2018) 16927–16931, https://doi.org/10.1021/acsami.7b18962.

[29] F. Sun, H. Markötter, D. Zhou, S.S.S. Alrwashdeh, A. Hilger, N. Kardjilov, I. Manke, J. Banhart, ChemSusChem 9 (2016) 946–950, https://doi.org/10.1002/cssc.201600220.

[30] J. Wang, Y.C.K. Chen-Wiegart, J. Wang, Angew. Chem. Int. Ed. 53 (2014) 4460–4464, https://doi.org/10.1002/anie.201310402.

[31] Q. Li, P. Wang, Q. Feng, M. Mao, J. Liu, S.X. Mao, H. Wang, Chem. Mater. 26 (2014) 4102–4108, https://doi.org/10.1021/cm5009448.

[32] X.H. Liu, J.Y. Huang, Energ. Environ. Sci. 4 (2011) 3844–3860, https://doi.org/10.1039/C1EE01918J.

[33] X.H. Liu, Y. Liu, A. Kushima, S. Zhang, T. Zhu, J. Li, J.Y. Huang, Adv. Energy Mater. 2 (2012) 722–741, https://doi.org/10.1002/aenm.201200024.

[34] J. Wang, F. Fan, Y. Liu, K.L. Jungjohann, S.W. Lee, S.X. Mao, X. Liu, T. Zhu, J. Electrochem. Soc. 161 (2014) F3019, https://doi.org/10.1149/2.0041411jes.

[35] A.F. Bower, P.R. Guduru, V.A. Sethuraman, J. Mech. Phys. Solids 59 (2011) 804–828, https://doi.org/10.1016/j.jmps.2011.01.003.

[36] R. Deshpande, Y.-T. Cheng, M.W. Verbrugge, A. Timmons, J. Electrochem. Soc. 158 (2011) A718, https://doi.org/10.1149/1.3565183.

[37] L.-Q. Chen, Annu. Rev. Mat. Res. 32 (2002) 113–140, https://doi.org/10.1146/annurev.matsci.32.112001.132041.

[38] B. Nestler, J. Cryst. Growth 204 (1999) 224–228, https://doi.org/10.1016/S0022-0248(99)00154-2.

[39] I. Steinbach, F. Pezzolla, B. Nestler, M. Seeßelberg, R. Prieler, G.J. Schmitz, J. L. Rezende, Physica D 94 (1996) 135–147, https://doi.org/10.1016/0167-2789(95)00298-7.

[40] Y.U. Wang, Y.M. Jin, A.G. Khachaturyan, J. Appl. Phys. 92 (2002) 1351–1360, https://doi.org/10.1063/1.1492859.

[41] M.Z. Bazant, Acc. Chem. Res. 46 (2013) 1144–1160, https://doi.org/10.1021/ar300145c.

[42] L. Chen, F. Fan, L. Hong, J. Chen, Y.Z. Ji, S.L. Zhang, T. Zhu, L.Q. Chen, Journal of The Electrochemical Society, 161 (2014) F3164-F3172. 10.1149/2.0171411jes.

[43] L. Chen, H.W. Zhang, L.Y. Liang, Z. Liu, Y. Qi, P. Lu, J. Chen, L.-Q. Chen, J. Power Sources 300 (2015) 376–385, https://doi.org/10.1016/j.jpowsour.2015.09.055.

[44] J.E. Guyer, W.J. Boettinger, J.A. Warren, G.B. McFadden, Phys. Rev. E 69 (2004), 021603, https://doi.org/10.1103/PhysRevE.69.021603.

[45] J.E. Guyer, W.J. Boettinger, J.A. Warren, G.B. McFadden, Phys. Rev. E 69 (2004), 021604, https://doi.org/10.1103/PhysRevE.69.021604.

[46] Z. Hong, V. Viswanathan, ACS Energy Lett. 3 (2018) 1737–1743, https://doi.org/10.1021/acsenergylett.8b01009.

[47] A. Jana, S.I. Woo, K. Vikrant, R.E. García, Energ. Environ. Sci. 12 (2019) 3595–3607, https://doi.org/10.1039/C9EE01864F.

[48] R.B. Smith, E. Khoo, M.Z. Bazant, J. Phys. Chem. C 121 (2017) 12505–12523, https://doi.org/10.1021/acs.jpcc.7b00185.

[49] N.J. de Klerk, A. Vasileiadis, R.B. Smith, M.Z. Bazant, M. Wagemaker, Physical Review Materials 1 (2017), 025404, https://doi.org/10.1103/PhysRevMaterials.1.025404.

[50] S. Hu, Y. Li, K.M. Rosso, M.L. Sushko, J. Phys. Chem. C 117 (2013) 28–40, https://doi.org/10.1021/jp3068014.

[51] A. Vasileiadis, N.J. de Klerk, R.B. Smith, S. Ganapathy, P.P.R. Harks, M.Z. Bazant, M. Wagemaker, Adv. Funct. Mater. 28 (2018) 1705992, https://doi.org/10.1002/adfm.201705992.

[52] J. Tiaden, B. Nestler, H.-J. Diepers, I. Steinbach, Physica D 115 (1998) 73–86, https://doi.org/10.1016/S0167-2789(97)00226-1.

[53] A. Khachaturyan, S. Semenovskaya, T. Tsakalakos, Phys. Rev. B 52 (1995) 15909, https://doi.org/10.1103/PhysRevB.52.15909.

[54] S.G. Kim, W.T. Kim, T. Suzuki, Phys. Rev. E 60 (1999) 7186, https://doi.org/10.1103/PhysRevE.60.7186.

[55] S.G. Kim, W.T. Kim, T. Suzuki, M. Ode, J. Cryst. Growth 261 (2004) 135–158, https://doi.org/10.1016/j.jcrysgro.2003.08.078.

[56] M. Plapp, Phys. Rev. E 84 (2011), 031601, https://doi.org/10.1103/PhysRevE.84.031601.

[57] A. Choudhury, B. Nestler, Phys. Rev. E 85 (2012), 021602, https://doi.org/10.1103/PhysRevE.85.021602.

[58] S. Daubner, P.K. Amos, E. Schoof, J. Santoki, D. Schneider, B. Nestler, Physical Review Materials 5 (2021), 035406, https://doi.org/10.1103/PhysRevMaterials.5.035406.

[59] S. Daubner, M. Weichel, D. Schneider, B. Nestler, Electrochim. Acta 421 (2022), 140516, https://doi.org/10.1016/j.electacta.2022.140516.

[60] L. Zhang, I. Steinbach, Acta Mater. 60 (2012) 2702–2710, https://doi.org/10.1016/j.actamat.2012.02.032.

[61] I. Steinbach, L. Zhang, M. Plapp, Acta Mater. 60 (2012) 2689–2701, https://doi.org/10.1016/j.actamat.2012.01.035.

[62] B. Nestler, H. Garcke, B. Stinner, Phys. Rev. E 71 (2005), 041609, https://doi.org/10.1103/PhysRevE.71.041609.

[63] J. Eiken, B. Böttger, I. Steinbach, Phys. Rev. E 73 (2006), 066122, https://doi.org/10.1103/PhysRevE.73.066122.

[64] A. Khachaturian, Theory of Structural Transformation in Solids (Wiley, New York, 1983), Chap. 8, p. 213.

[65] I. Steinbach, F. Pezzolla, Physica D 134 (1999) 385–393, https://doi.org/10.1016/S0167-2789(99)00129-3.

[66] H.-C. Yu, H.-Y. Chen, K. Thornton, Model. Simul. Mater. Sci. Eng. 20 (2012), 075008, https://doi.org/10.1088/0965-0393/20/7/075008.

[67] G.E. Crooks, J. Stat. Phys. 90 (1998) 1481–1487, https://doi.org/10.1023/A:1023208217925.

[68] C. Jarzynski, Phys. Rev. Lett. 78 (1997) 2690, https://doi.org/10.1103/PhysRevLett.78.2690.

[69] J.A. Gilbert, I.A. Shkrob, D.P. Abraham, J. Electrochem. Soc. 164 (2017) A389, https://doi.org/10.1149/2.1111702jes.

[70] S. Nowak, M. Winter, Acc. Chem. Res. 51 (2018) 265–272, https://doi.org/10.1021/acs.accounts.7b00523.

[71] C. Zhan, X. Qiu, J. Lu, K. Amine, Adv. Mater. Interfaces 3 (2016) 1500856, https://doi.org/10.1002/admi.201500856.

[72] L. Chang, Y. Lu, L. He, Y. Ni, Int. J. Solids Struct. 143 (2018) 73–83, https://doi.org/10.1016/j.ijsolstr.2018.02.033.

[73] L.Q. Chen, J. Shen, Comput. Phys. Commun. 108 (1998) 147–158, https://doi.org/10.1016/S0010-4655(97)00115-X.

[74] W. Blase, G. Cordier, Zeitschrift für Kristallographie - Crystalline Materials 193 (1990) 317–318, https://doi.org/10.1524/zkri.1990.193.3-4.317.
[75] U. Frank, W. Müller, Zeitschrift für Naturforschung B 30 (1975) 316–322, https://doi.org/10.1515/znb-1975-5-605.
[76] U. Frank, W. Müller, H. Schäfer, Zeitschrift für Naturforschung B 30 (1975) 6–9, https://doi.org/10.1515/znb-1975-1-203.
[77] D. Hansen, L. Chang, Acta Crystallographica Section B: Structural Crystallography and Crystal, Chemistry 25 (1969) 2392–2395, https://doi.org/10.1107/S0567740869005760.
[78] W. Müller, H. Schäfer, Zeitschrift für Naturforschung B 28 (1973) 246–248, https://doi.org/10.1515/znb-1973-5-604.
[79] G. Kresse, J. Furthmüller, Comput. Mater. Sci 6 (1996) 15–50, https://doi.org/10.1016/0927-0256(96)00008-0.
[80] P.E. Blöchl, Phys. Rev. B 50 (1994) 17953, https://doi.org/10.1103/PhysRevB.50.17953.
[81] J.P. Perdew, K. Burke, M. Ernzerhof, Phys. Rev. Lett. 77 (1996) 3865, https://doi.org/10.1103/PhysRevLett.77.3865.
[82] Y. Du, J.C. Schuster, Metall. Mater. Trans. A 32 (2001) 2396–2400, https://doi.org/10.1007/s11661-001-0214-7.
[83] A.T. Dinsdale, Calphad 15 (1991) 317–425, https://doi.org/10.1016/0364-5916(91)90030-N.
[84] J. Gao, S.-Q. Shi, H. Li, Chin. Phys. B 25 (2015), 018210, https://doi.org/10.1088/1674-1056/25/1/018210.
[85] C.S. Hong, N. Qaiser, H.G. Nam, S.M. Han, PCCP 21 (2019) 9581–9589, https://doi.org/10.1039/C9CP00559E.
[86] E. Schoof, D. Schneider, N. Streichhan, T. Mittnacht, M. Selzer, B. Nestler, Int. J. Solids Struct. 134 (2018) 181–194, https://doi.org/10.1016/j.ijsolstr.2017.10.032.
[87] B. Lu, Y. Song, Q. Zhang, J. Pan, Y.-T. Cheng, J. Zhang, PCCP 18 (2016) 4721–4727, https://doi.org/10.1039/C5CP06179B.
[88] C. Jin, H. Li, Y. Song, B. Lu, A. Soh, J. Zhang, Sci. China Technol. Sci. 62 (2019) 1357–1364, https://doi.org/10.1007/s11431-018-9491-6.
[89] G. Bucci, T. Swamy, S. Bishop, B.W. Sheldon, Y.-M. Chiang, W.C. Carter, J. Electrochem. Soc. 164 (2017) A645, https://doi.org/10.1149/2.0371704jes.
[90] S. Huang, F. Fan, J. Li, S. Zhang, T. Zhu, Acta Mater. 61 (2013) 4354–4364, https://doi.org/10.1016/j.actamat.2013.04.007.